JGR Solid Earth

Key Points:

- The effects of 3D sediments, lithosphere, upper mantle (anelastic) on ocean tide loading and ocean tide dynamics have been studied here
- The inclusion of these 3D earth features leads to an improvement of predicted vertical M_2 displacements as confirmed with Global Navigation Satellite System observations
- The potential impact of changes in displacement on tidal systems is amplified, especially for semidiurnal tides (e.g., 6 mm for M_2)

Correspondence to:

P. Huang,
pingping.huang@newcastle.ac.uk

Author Contributions:

Conceptualization: Pingping Huang, Roman Lucas Sulzbach, Volker Klemann, Henryk Dobslaw
Funding acquisition: Maik Thomas
Methodology: Pingping Huang, Roman Lucas Sulzbach
Project Administration: Maik Thomas
Software: Yoshiyuki Tanaka, Zdeněk Martinec
Supervision: Volker Klemann, Henryk Dobslaw

The Influence of Sediments, Lithosphere and Upper Mantle (Anelastic) With Lateral Heterogeneity on Ocean Tide Loading and Ocean Tide Dynamics

Pingping Huang[1,2] , Roman Lucas Sulzbach[1,3] , Volker Klemann[1] , Yoshiyuki Tanaka[4], Henryk Dobslaw[1] , Zdeněk Martinec[5,6], and Maik Thomas[1,3]

[1]German Research Center for Geosciences, Department 1 Geodesy, Potsdam, Germany, [2]School of Engineering, Newcastle University, Newcastle Upon Tyne, UK, [3]Freie Universität Berlin, Institute of Meteorology, Berlin, Germany, [4]Earth and Planetary Sciences, The University of Tokyo, Tokyo, Japan, [5]Dublin Institute for Advanced Studies DIAS, Dublin, Ireland, [6]Charles University, Faculty of Mathematics and Physics, Prague, Czech Republic

Abstract Ocean tide loading (OTL) and ocean tide dynamics (OTD) are known to be affected by Earth's internal structures, with the latter being affected by the self-attraction and loading (SAL) potential. Combining the 3D earth models Lyon and LITHO1.0, we construct a hybrid model to quantify the coupled effect of sediments, oceanic and continental lithosphere, and anelastic upper mantle on OTL and OTD. Compared to PREM, this more realistic 3D model produces significantly larger vertical OTL displacement by up to 3.9, 2.6, and 0.1 mm for the M_2, K_1, and M_f OTL, respectively. Moreover, it shows a smaller vector difference of 0.1 mm and a smaller amplitude difference of 0.2 mm than PREM with OTL observations at 663 Global Navigation Satellite System stations, a confirmation of the cumulative effect due to these earth features. On the other hand, we find a resonant impact of wider extent and larger magnitude on OTD, especially for the M_2 and K_1 tides. Specifically, this impact is concentrated in the ranges 0–6 mm and 0–1.5 mm for M_2 and K_1, respectively, which is considerably larger than the impact on SAL (mostly in the ranges 0–2 mm and 0–1.0 mm, respectively). Since the effect on vertical displacement is at a similar level compared to the accuracy of modern data-constrained ocean tide models that require correction of the geocentric tide by loading induced vertical displacements, we regard its consideration to be potentially beneficial in OTD modeling.

Plain Language Summary The whole earth body deforms under loading processes like ocean tide loading. The knowledge of its internal structure is mandatory to model its deformational behavior. Here, we apply realistic structures of the lithosphere and mantle which change from place to place. Furthermore, we consider that the material behavior is not purely elastic, but becomes weaker when the loading process lasts longer to the periods of ocean tides such as half a day, 1 day and 14 days. We model the deformation with an advanced earth model code and discuss the influence of these features on Earth's deformation and how the deformation influences the ocean tides themselves. We confirm our results with Global Navigation Satellite System observations using coastal and inland stations. Our conclusion is that one has to consider the influence of these structural features when modeling tidal loading and the tidal dynamics itself.

1. Introduction

Ocean tide loading (OTL) refers to the periodic redistribution of water masses in the ocean, which is driven by gravitational forces from celestial bodies such as the Sun and Moon, and results in deformations of the solid Earth and perturbations of its gravity field. Recent studies on OTL (e.g., Bos et al., 2015; Martens, Rivera, et al., 2016; Martens & Simons, 2020; Martens, Simons, et al., 2016; Matviichuk et al., 2021; Wang et al., 2020) find limitations in one-dimensional (1D) elastic/anelastic earth models for explaining OTL displacements observed by the Global Navigation Satellite Systems (GNSSs). Using jointly inverted Q (seismic quality factor) and Vs (S wave velocity) models of Earth's upper mantle, Huang et al. (2021) constructed three-dimensional (3D) anelastic earth models (spherical earth models with material properties varying in both vertical and horizontal directions) and used them to study OTL displacements with the hydrodynamic ocean tide model TiME (Sulzbach et al., 2021). They showed the widespread effect of anelasticity on OTL displacements caused by the M_2 tide, and found that the impact of lateral heterogeneity on OTL displacement is relatively high in the coastal areas of north Australia as well as North and Central America. In addition, they found a similar impact of anelasticity and lateral

Writing – original draft: Pingping Huang, Roman Lucas Sulzbach
Writing – review & editing: Volker Klemann, Yoshiyuki Tanaka, Henryk Dobslaw, Zdeněk Martinec, Maik Thomas

heterogeneity on self-attraction and loading (SAL) elevation, and more importantly, they showed that this impact has a feedback to OTD with an root-mean-square (RMS) of above 5 mm in specific coastal areas. However, there are several aspects missing in the 3D anelastic earth models of Huang et al. (2021) as well as the 1D elastic/anelastic earth models used in other OTL studies, which include 3D sediments, oceanic and continental lithosphere and anelasticity for longer-period OTL such as the K_1 and M_f tides. This study will focus on these three aspects of the solid Earth and show their impact on OTL and OTD. In particular, the effects of sediments and oceanic/continental lithosphere will be explored systematically because the shallow structure of the Earth such as the crust can significantly affect the localized deformations due to hydrological loading (e.g., Dill et al., 2015).

Starting from the surface of the solid Earth, the effect of sediments is often not considered in OTL studies although it is well established that the sediment rock has rather low densities and seismic velocities, leading to a weak structure overlying the crust (Laske & Masters, 1997; Mooney et al., 1998). The thickness of sediments varies with geographic locations from a few hundred meters in open ocean areas to several kilometers in coastal areas and more than 20 km in the north Caspian Sea (Pasyanos et al., 2014). Incorporating sediments into the surface mass loading problem has been done in studies such as Simms et al. (2007) and Dalca et al. (2013), where sediments are treated as surface loads that impose deformational, gravitational and rotational effects on postglacial sea level change. Different from that treatment, in the scenario of OTL it is more natural to treat sediments as a part of the solid Earth (Laske & Masters, 1997; Mooney et al., 1998; Pasyanos et al., 2014) that undergoes gravitational change and deformation. Given the timescale of tidal loading considered here, ranging from ∼12 hr to ∼14 days, which is much shorter than the timescale of other geodynamic processes such as Glacial Isostatic Adjustment (∼100 thousand years) and plate motion (more than 1 million years), we consider an elastic deformation rather than a viscoelastic or visco-elasto-plastic deformation in sediments.

Regarding the lithospheric structures, inverse modeling studies using gravity, seismic and heat flow data reveal relatively low crustal densities and (seismic) velocities of the mid-ocean ridges (MORs) and continents, associated with high temperature, young age and chemical compositions, but relatively high velocities and densities in ocean regions away from the MORs, related to low temperature, old age and chemical compositions (e.g., Afonso et al., 2019; Fullea et al., 2021; Schaeffer & Lebedev, 2013). In the lithospheric mantle, low densities and velocities are not restricted to the MORs, but are more widespread in ocean areas, whereas high densities and velocities are dominant in continental interiors. The elastic moduli of the Earth's lithosphere (including both the crust and the lithospheric mantle) calculated from the density and seismic velocity, thus exhibit strong lateral variations. The global 1D reference elastic earth models such as PREM (Dziewonski & Anderson, 1981), AK135 (Kennett et al., 1995) and STW105 (Kustowski et al., 2008) represent spherical average Earth properties by neglecting this variability. As a result, the strength of the crust is in general overestimated at the MORs and continental regions, but underestimated in ocean regions away from the MORs. In the lithospheric mantle (lid), the strength is overestimated over more ocean areas including the MORs, but underestimated over continental regions. The local 1D models constructed in OTL studies (e.g., Bos et al., 2015; Martens & Simmons, 2020; Matviichuk et al., 2021; Wang et al., 2020) to mimic the regional earth structure below GNSS stations can be an alternative to the global 1D model, but they still neglect the impact of lateral heterogeneity (e.g., Huang et al., 2021). Without comparing the modeled OTL/OTD results based on these 1D local models with solutions based on 3D global models where the impact of lateral heterogeneity is included, it is not rigorous to declare the 1D local model as an optimum. Moreover, limited number of 1D local models cannot be applied in a global study with high resolutions such as ours (a resolution of 0.089°). Therefore, to accurately model global OTL displacements, it is necessary to consider a more realistic 3D lithosphere model with deviating features between continents and oceans. Naturally, the oceanic lithosphere structure right below the oceans has to be considered as well as the continental structure which considerably affects OTL displacements through the impact of lateral heterogeneity (Huang et al., 2021).

A further aspect is the consideration of anelasticity in the upper mantle where seismic attenuation is much higher than in other parts of the solid Earth (Karaoğlu & Romanowicz, 2018). Elastic earth models such as PREM, AK135 or STW105 used in OTL studies are defined for a reference frequency usually in the range of ∼10^{-3} to 100 Hz. This seismic frequency band is substantially above the tidal band starting at ∼10^{-5} Hz, and so whether to use such elastic earth models for OTL studies is under debate (Bos et al., 2015; Huang et al., 2021; Ivins et al., 2020; Martens and Simons, 2020; Wang et al., 2020). Seismic tomography/attenuation studies clearly show the frequency dependence of P and S wave velocities (Vp and Vs, respectively), that is, the dispersion of seismic velocities, implying that the elastic moduli characterizing the mechanical properties of rocks also depend on frequency, at least, in the seismic band. Furthermore, mineral and rock physics reveal that, at high

temperatures the elastic moduli of rocks as well as attenuation (Q^{-1}) depend on the frequency (period) of externally applied forces. This frequency-dependent behavior is usually attributed to anelasticity, a manifestation of the relaxation process inside the rock which is characterized by an intrinsic relaxation timescale and strength. Recent forced oscillation tests of rock or rock analogy (e.g., Jackson et al., 2002, 2004; Takei, 2017; Takei et al., 2014; Yamauchi & Tekei, 2016) with frequencies $2-10^{-4}$ Hz have shown that the frequency dependence of elastic moduli and attenuation can be explained by a continuum spectrum plus a peak. The former is called the high-temperature background (HTB), closely fitted by a power law (with the power $\alpha = 0.20-0.40$) and dominating the anelastic effect. Clearly, the HTB is consistent with the classical α law proposed by Anderson and Minster (1979). The latter (peak) is related to temperature and melt fraction of rock. Since frequencies $2-10^{-4}$ Hz used in laboratory studies are still higher than tidal frequencies, it is unclear what the anelastic law looks like in the tidal band. However, the anelastic effect must be considered at tidal frequencies. Moreover, considering the limitations in elastic earth models for explaining GNSS observations of the OTL displacements, it is worthwhile to extrapolate the classical α law to OTL frequencies. Following this reasoning, Huang et al. (2021) constructed 3D anelastic earth models with the α law extrapolated to the tidal frequency of M_2 (2.2×10^{-5} Hz). Here, the α law is assumed to be applicable to a lower frequency of the M_f tide (8.4×10^{-7} Hz), for which we expect a further increase of shear relaxation.

OTL studies usually focus on the impact of ocean tides on the solid Earth, that is, causing deformation and gravity change. However, the solid Earth influences ocean tides through the SAL potential, a secondary tide-generating potential (e.g., Ray, 1998; Schindelegger et al., 2018; Schwiderski, 1980). The SAL elevation, that is, the SAL potential divided by the surface gravity describes the geoid perturbation due to self-attraction of ocean mass redistributions and deformation of the solid Earth with respect to the ground vertical displacement due to OTL. To avoid the high numerical cost of global convolution integrals at each time step for SAL calculations, many numerical ocean tide models traditionally used an approximation based on a constant fraction of the tidal elevation (e.g., Weis et al., 2008) or an updated tidal analysis approach (e.g., 5 iterations). With the Love number approach (e.g., Sulzbach et al., 2021), the SAL elevation for 1D elastic/anelastic solid earth models can be updated dynamically for each time step and self-consistently included into the OTD modeling (Huang et al., 2021). In Huang et al. (2021), the perturbation of the SAL elevation caused by lateral heterogeneities in Earth's structures for the M_2 tide was also computed and treated as a static force in tidal modeling. In addition, for the first time, the impact of anelasticity on SAL and further on the M_2 tide were estimated there. Here, in addition to the anelastic effect of the upper mantle, we will consider the impact of more realistic 3D sediment and lithosphere structures on the M_2 tide as well as longer-period tides such as the daily K_1 and fortnightly M_f.

The following section will describe the 3D sediment, lithosphere, upper mantle models as well as the ocean tide model adopted in this study. We will introduce the hybrid earth models constructed by replacing PREM's lithosphere or (and) upper mantle by the 3D models. In addition, the structure deviation of the 3D model from PREM, the methods and spatial resolutions used to model OTL and the means of accounting for SAL feedback to OTD will be discussed. In Section 3, we will show and discuss OTL displacements, SAL elevations and the SAL feedback to OTD based on newly-constructed earth models as well as comparing modeled OTL displacements with GNSS observations. Conclusions will be presented in Section 4.

2. Models and Methods

2.1. Solid Earth Model Construction

Our approach is to construct hybrid solid earth models by using PREM (valid at 1 Hz) as the basis model. PREM is selected because it is widely used in OTL and OTD studies. In constructing hybrid models, the mechanical structure (characterized by elastic moduli) of the lower mantle and core was set to be identical to PREM but the mechanical structure of the lithosphere or (and) the upper mantle was replaced by 3D models. In addition, the density structure of the hybrid models is set to that of PREM. Martens, Simons, et al. (2016) showed that OTL displacements are weakly sensitive to density variations but strongly sensitive to elastic moduli variations at depths 0–500 km. Therefore, density deviations from PREM and mechanical structure deviations from PREM in the lower mantle and core with depths >500 km are not crucial. In addition, we considered anelasticity in the upper mantle and not in the lithosphere because seismic attenuation is relatively high in the former and low in the latter (Karaoğlu & Romanowicz, 2018). Moreover, different from the thermal, electrical or chemical lithospheres defined in inversion studies (e.g., Artemieva, 2011; Fullea et al., 2021), we chose a mechanical/seismic

Table 1
The 3D Sediment, Lithosphere and Upper Mantle Models Which Are Used as Components in This Study

Structure	Models for Earth's individual structures				
	Sediments (elastic, 3D)		Lithosphere (elastic, 3D)		Upper mantle (anelastic, 3D)	Lower mantle (elastic, 1D) + core (fluid, 1D)
Model	LITHO1.0	newSed	LITHO1.0	WINTERC-G	Lyon	sPREM

Note. Note that sPREM is a model with only lower mantle and core structures of PREM.

lithosphere with a depth range of 0–80 km and an upper mantle with depths 80–670 km, which is consistent with PREM. Due to this, only densities and seismic velocities in the corresponding depth range were taken from the 3D lithosphere and upper mantle models.

As will be shown in the following sections, we consider three 3D lithosphere models (with or without sediments), namely, LITHO1.0 (Pasyanos et al., 2014), LITHO1.0−newSed (see Section 2.1.1 for details) and WINTERC-G (Fullea et al., 2021), and one 3D anelastic upper mantle model, namely, Lyon (see Section 2.1.2 for definition). The lower mantle, considered as being 1D, is taken from PREM and denoted as sPREM (Table 1). To simplify our descriptions, we name the hybrid model constructed with LITHO1.0, a second hybrid model with LITHO1.0-newSed and a third hybrid model with WINTERC-G as LH-3De, LH-nS-3De and WG-3De, respectively, and a fourth hybrid model with Lyon as Lyon-3Dae. Moreover, we constructed a hybrid model with structures from both LITHO1.0 and Lyon, and name it LH-Lyon-3Dae. The global average of LH-Lyon-3Dae is called LH-Lyon-1Dae. Tables 1 and 2 show a summary of these models. In the following, we will show in detail, how more realistic 3D lithosphere and upper mantle structures deviate from PREM.

2.1.1. The 3D Elastic Lithosphere Models

Two recent 3D global lithosphere models, WINTERC-G (Fullea et al., 2021) and LITHO1.0 (Pasyanos et al., 2014), were considered here. WINTERC-G is a thermochemical model of the lithosphere (without sediments) and upper mantle down to a depth of 400 km, including information about density, seismic velocity and thickness. It is constrained by satellite gravimetry, seismic and heat flow data and is represented on a triangular grid with an average spacing of 225 km. LITHO1.0 is a 1° tessellated model including density, velocity and thickness information for the sediments, crust and uppermost mantle. It is created to fit surface wave data in a wide frequency range of 5–40 mHz and by choosing CRUST1.0 (Laske et al., 2013) as the starting model. Apart from these two lithosphere models, we considered an updated sediment model of continents (Europe, North America, Asia, Australia, Antarctica) and oceans, namely, newSed, with density and thickness information collected from the literature (Divins, 2003; Haeger et al., 2019; Kaban et al., 2010, 2016; Whittaker et al., 2013). In a further lithosphere model LITHO1.0−newSed we replaced the sedimentary thickness and density in LITHO1.0 with those in newSed. Because a spherical solid earth model was considered here, we filled in the ocean depths (in general the first 5–6 km) with the underlying sediment or upper crust (mechanical) structure in all considered lithosphere models (e.g., Bos et al., 2015). The total mass of the Earth is conserved because PREM's density structure (Dziewonski & Anderson, 1981) is used in all hybrid 1D and 3D models.

Figure 1a shows the global distribution of the total sediment thickness in LITHO1.0. This model includes one to three oceanic sediment layers. The open ocean areas are usually represented by one layer with sediments thinner than 500 m, while the continental-shelf areas (e.g., those of Russia, the Americas and Africa) have two or three layers with 1–10 km thick sediments. The first oceanic sediment layer of LITHO1.0 usually consists of thin (in general less than 1 km) and unconsolidated or weak material, which makes the OTL displacement solutions unstable; thus, we replaced the first sediment layer with the underlying sediment or upper crust structure. Accordingly, sediments in most open ocean areas (with only one layer) were not considered. Figure 1b shows the shear modulus distribution of LITHO1.0 at a sediment depth of 1 km. It can be observed that the shear modulus is ~60%–80% smaller than that of PREM in coastal areas with thick sediments, and ~40% smaller in open ocean areas (note: it is the shear modulus from the underlying upper crust structure). Figures 1c and 1d show the shear modulus of LITHO1.0 at the upper and lower crust depths, 11 and 25 km, respectively. In comparison to the more realistic 3D lithosphere model, PREM underestimates the shear modulus of the oceanic crust (~10–30 km thick) by more than 60% in regions away from MORs. In the upper oceanic crust, the underestimation can exceed 150%, occurring at a thickness of ~3 km. Be also aware that PREM overestimates the shear modulus of the lower crust by

Table 2
The Resulting Hybrid Earth Models

		Hybrid Earth models				
Combined models	LITHO1.0 + sPREM	LITHO1.0 + newSed + sPREM	WINTERC-G + sPREM	Lyon + sPREM	LITHO1.0 + Lyon + sPREM	LITHO1.0 + Lyon + sPREM
Short hybrid-model name	LH-3De	LH-nS-3De	WG-3De	Lyon-3Dae	LH-Lyon-3Dae	LH-Lyon-1Dae

Note. Notice that the last model LH-Lyon-1Dae is the global mean of the 3D model LH-Lyon-3Dae.

~5%–20% in continents and some continental-shelf regions (coinciding with the location of sediments). Shown in Figure 1e is the shear modulus of LITHO1.0 at the lid depth 78 km. Again, compared to LITHO1.0, PREM underestimates the shear modulus of the oceanic lid (only a thickness of ~45–65 km considered in this study) by up to ~7%, but in less open ocean areas away from the MORs (compare Figures 1c and 1e), and overestimates the shear modulus by ~10%–18%, but in more open ocean areas in and close to the MORs (compare Figures 1c and 1e). Also note that PREM underestimates the shear modulus of the lid layer in continental interiors.

As a comparison to the sediment and lithosphere structures in LITHO1.0, we show the shear modulus and thickness of newSed in Figure S1a in Supporting Information S1, and the shear modulus in WINTERC-G at three depths, that is, 11 km (upper crust), 24 km (lower crust) and 78 km (lid) in Figure S1b in Supporting Information S1. Comparison of Figures 1a and 1b with Figure S1a in Supporting Information S1 shows that, with respect to LITHO1.0, newSed has slightly different sedimentary thicknesses in the coasts of Antarctica, Africa and Pakistan, thinner sediments at the northern coast of Australia, and thicker sediments in the North Sea, the Norwegian Sea and the continental shelf regions of Ireland and the UK. Moreover, newSed in general exhibits a weaker sediment structure than LITHO1.0 in ocean areas except for the Gulf of Mexico, the inner coastal areas of eastern United States and Venezuela, where newSed is slightly stronger (~3%–10%). Comparing Figure S1b in Supporting Information S1 with Figures 1c–1e reveals that WINTERC-G is similar to LITHO1.0 in terms of the shear-modulus distribution (compare the pattern), but with a much greater magnitude in ocean areas including the MORs. For example, in most ocean areas at the 11 km depth, the shear modulus in WINTERC-G is ~130%–170% larger (Figure S1b in Supporting Information S1) than that of PREM, while the shear modulus in LITHO1.0 is only ~60%–70% larger (Figure 1c). More importantly, the shear strength shown at depth 11 km exists at a thickness of ~7–9 km for WINTERC-G but a thickness of only ~3 km for LITHO1.0. Due to this, WINTERC-G is significantly stronger than LITHO1.0 under the oceans.

2.1.2. The 3D Anelastic Upper Mantle Model

The anelastic upper mantle model (containing 3D elastic and anelastic structures) in this study follows that of Huang et al. (2021). Therein, we derived anelastic mantle models at the M_2 frequency from two seismic tomography models, SEMUCB-UMQ (Karaoğlu & Romanowicz, 2018) from the University of California, Berkeley, and DR2020s (QsADR17) (Adenis et al., 2017; Debayle et al., 2020) from the École normale supérieure de Lyon. In both models, the quality factor Q as well as V_S was jointly inverted for. To derive the corresponding relaxation of the elastic parameters we applied the classical Q-α attenuation model: from the seismic reference frequency $w_0 = 1$ Hz to the tidal frequency w, the bulk modulus is kept unchanged (due to low bulk attenuation), while the shear modulus (μ) is reduced and calculated by (e.g., Benjamin et al., 2006)

$$\delta\mu(w) = \frac{\mu_0}{Q_0}\left\{\frac{2}{\pi}\left[ln\left(\frac{w_m}{w_0}\right) + \frac{1}{\alpha}\left(1 - \left(\frac{w_m}{w}\right)^{\alpha}\right)\right] + i\left(\frac{w_m}{w}\right)^{\alpha}\right\}. \tag{1}$$

This equation is derived on the basis that Q is constant in the seismic frequency band $[w_0, w_m]$ with $w_m = 2\pi \times 3.09 \times 10^{-4}$ rad/s, the frequency of the longest-period free oscillation of the Earth, but depends on frequency in the band $[w_m, w]$. In Equation 1, μ_0 and Q_0 are the values of μ and Q valid at w_0, respectively, and $\alpha = 0.25$. Since the Berkeley and Lyon models have a similar impact on OTL and OTD (Huang et al., 2021), we adopted only the Lyon model here and determined the change in shear modulus, $\delta\mu$ at two lower frequencies, that is, the frequencies of the daily K_1 and fortnightly M_f. Note that, we neglect the imaginary component of $\delta\mu$ due to its small impact on modeled displacement (Bos et al., 2015).

Figure 2 shows the variation of shear modulus from the frequency of 1 Hz to those of M_2 (Figure 2a), K_1 (Figure 2b) and M_f (Figure 2c) tides, based on the 3D anelastic Lyon model. A large reduction of the shear modulus at the MORs or below hot spots can be observed from the figure, which is associated with high attenuation. And, apparently, the anelastic effect increases with the period of tidal loading, for example, at the 135 km depth the maximum shear modulus difference (in craton regions where Q_0 is large) between the 3D Lyon model and PREM decreases from 21.0% to 20.0% and its minimum difference (at the MORs or below hot spots where Q_0 is small) from −36.7% to −60.8%, when the tidal period increases from 12.42 hr to 13.66 days.
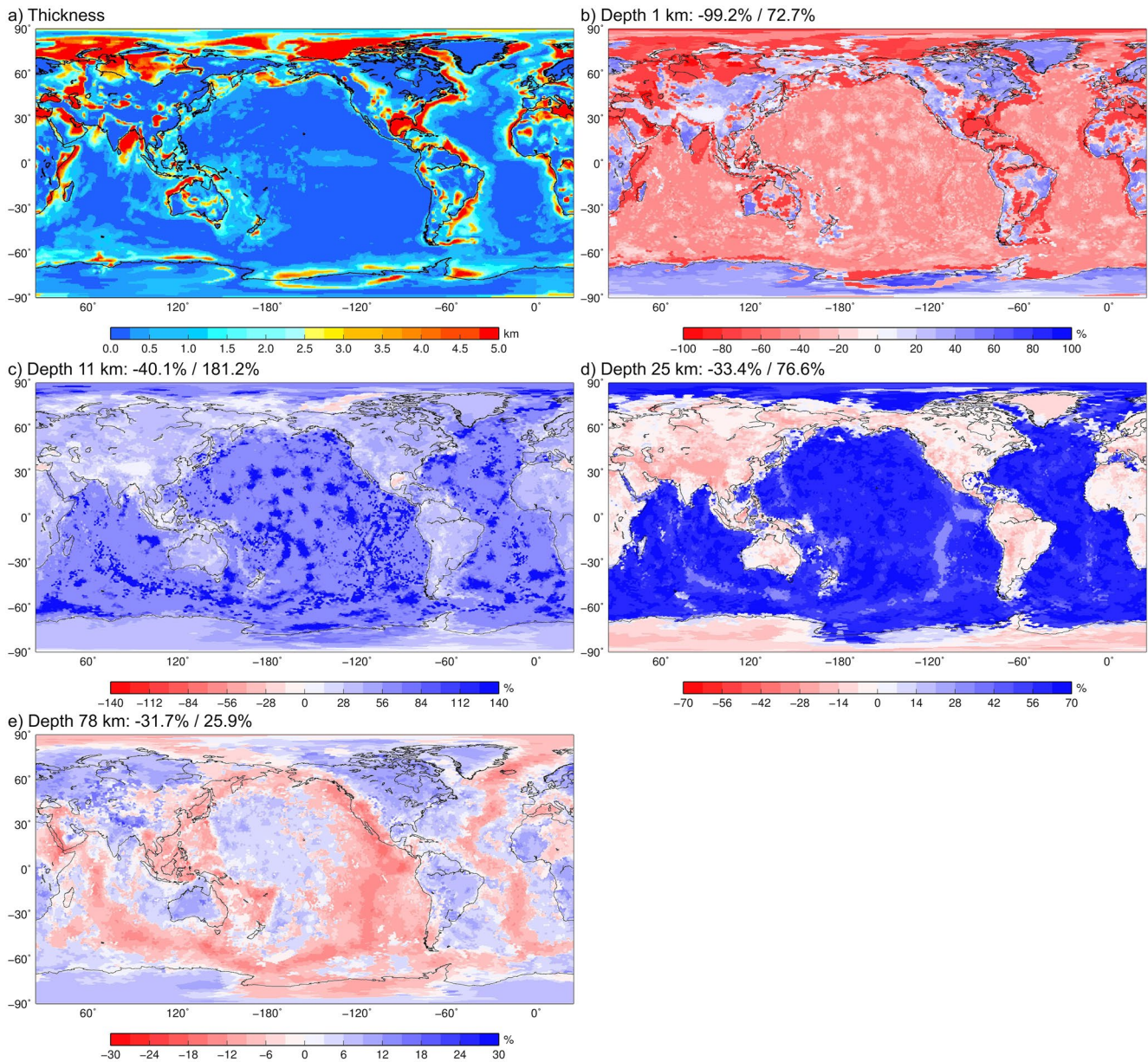
Figure 1. Total sediment thickness of LITHO1.0 (a) and the shear modulus comparison (in percentage) between LITHO1.0 and PREM at the selected sedimentary depth 1 km (b), the upper crustal depth 11 km (c), the lower crust depth 25 km (d) and the lid depth 78 km (e). Shown above the subplot are the maximum positive and negative differences.

2.2. The Ocean Tide Model

For OTL modeling, we adopted the ocean tide model TiME (Sulzbach et al., 2021) that was also used by Huang et al. (2021). While not being satellite data-constrained, TiME constructs ocean tide solutions by the means of hydrodynamic modeling on a regular longitude/latitude grid with a resolution of 1/12° that is reduced at two given latitude circles toward the numerical poles, which are rotated to antipodic, dry grid cells located in South America and East Asia. This rotated numerical grid allows both the avoidance of the coordinate singularity at the numerical poles and the implementation of a relatively long time step of close to 180 s (the exact values are identical to those of Shihora et al., 2022). The model self-consistently includes the SAL feedback from OTL on a 1D Earth model–PREM by combining the respective load Love numbers (LLNs) (Wang et al., 2012) with the sea surface elevation in the spectral domain. In addition, the model considers tidal energy dissipation by quadratic bottom friction, parametrized eddy-viscosity and parametrized generation of internal tides (topographic
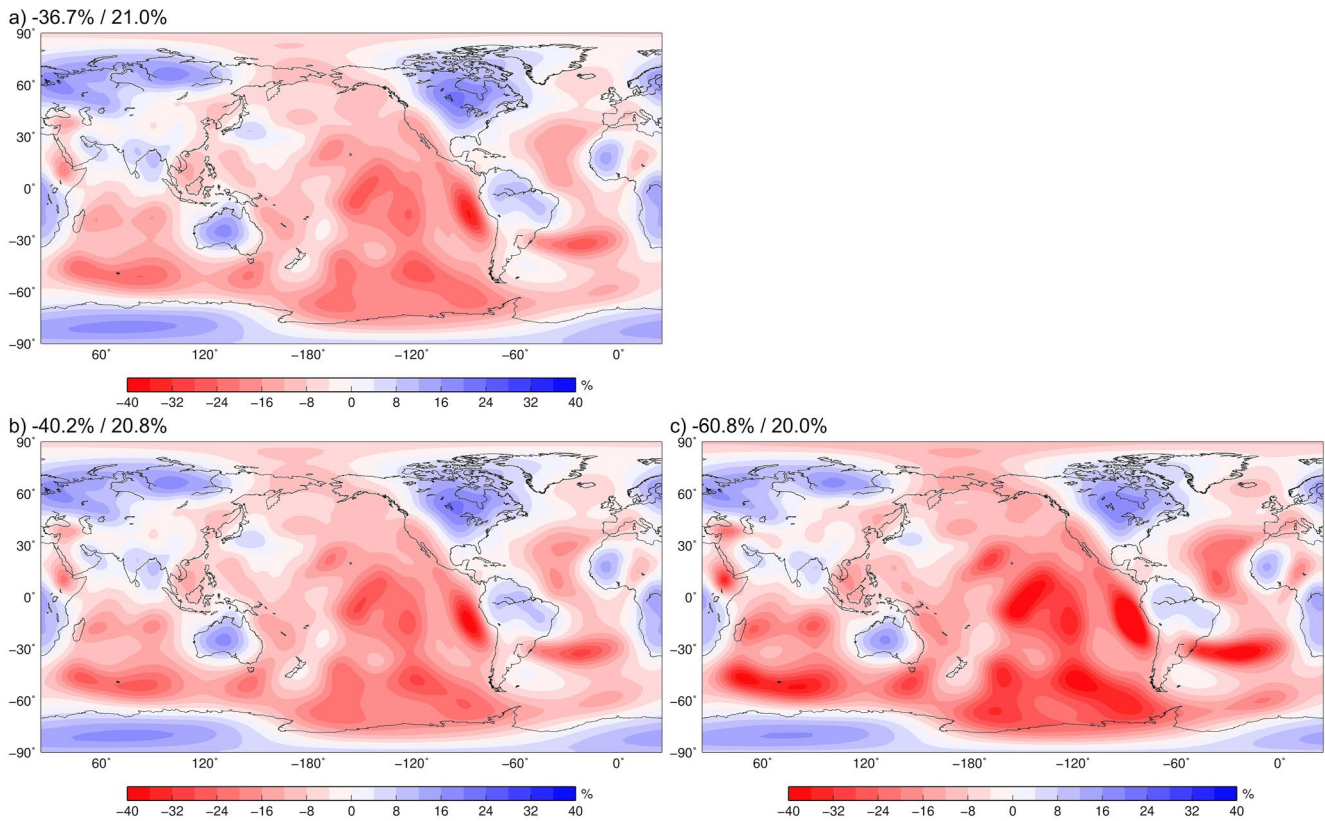
Figure 2. The shear modulus comparison (in percentage) at a depth of 135 km between the 3D anelastic Lyon model (see the text for definition) and PREM (valid at 1 s), at the frequencies of M_2 (a), K_1 (b) and M_f (c). The maximum positive and negative differences are given above each panel.

wave drag). While, in general, TiME considers nonlinear effects (advection, bottom-friction, wave drift), all tidal modeling in this study has been performed in partial tide forcing-mode, that is, only considering tide-raising forces at a certain frequency, degree and order obtained from the HW95 Tide-Generating Potential (Hartmann & Wenzel, 1995) and harmonically analyzing the model output for the exact same frequency. This approach neglects possible nonlinear interactions between individual partial tides that can introduce minor modifications of the obtained tidal solutions. This can be motivated with the following comparison: the interaction of two major tides is proportional to the amplitudes of the two constituents (e.g., $M_2 + M_2 \rightarrow M_4$) and produces nonlinear corrections with coastal mean amplitudes in the few-cm regime (e.g., Lyard et al., 2021). The nonlinear backaction to the respective major tide (e.g., $M_2 + M_4 \rightarrow M_2$) is more reduced and in the sub-cm regime, which is negligible compared to the accuracy of TiME (Sulzbach et al., 2021). As the model output is strictly periodic, we take the global in-phase and quadrature components of the individual M_2, K_1 or M_f runs as the surface loads for the OTL modeling.

Figure 3 shows the amplitude and phase for the M_2, K_1, and M_f tides, from which can be seen a decreasing trend in the magnitude of OTL with the period increasing from semi-diurnal (M_2) to fortnight (M_f). A different ocean tide model is not used here because we focus on exploring the impact of variability in the solid-earth structure on OTL and OTD.

2.3. Methods

2.3.1. OTL Modeling

We applied the spectral-finite element method (Martinec, 2000) to model OTL-induced displacement and potential, which was initially developed for a Maxwell rheology allowing for lateral variations in viscosity (Bagge et al., 2021; Klemann et al., 2008). It was then modified to consider lateral changes in elasticity with an iterative approach (Huang et al., 2021; Tanaka et al., 2019). This spectral code VILMA-E is further updated here to a
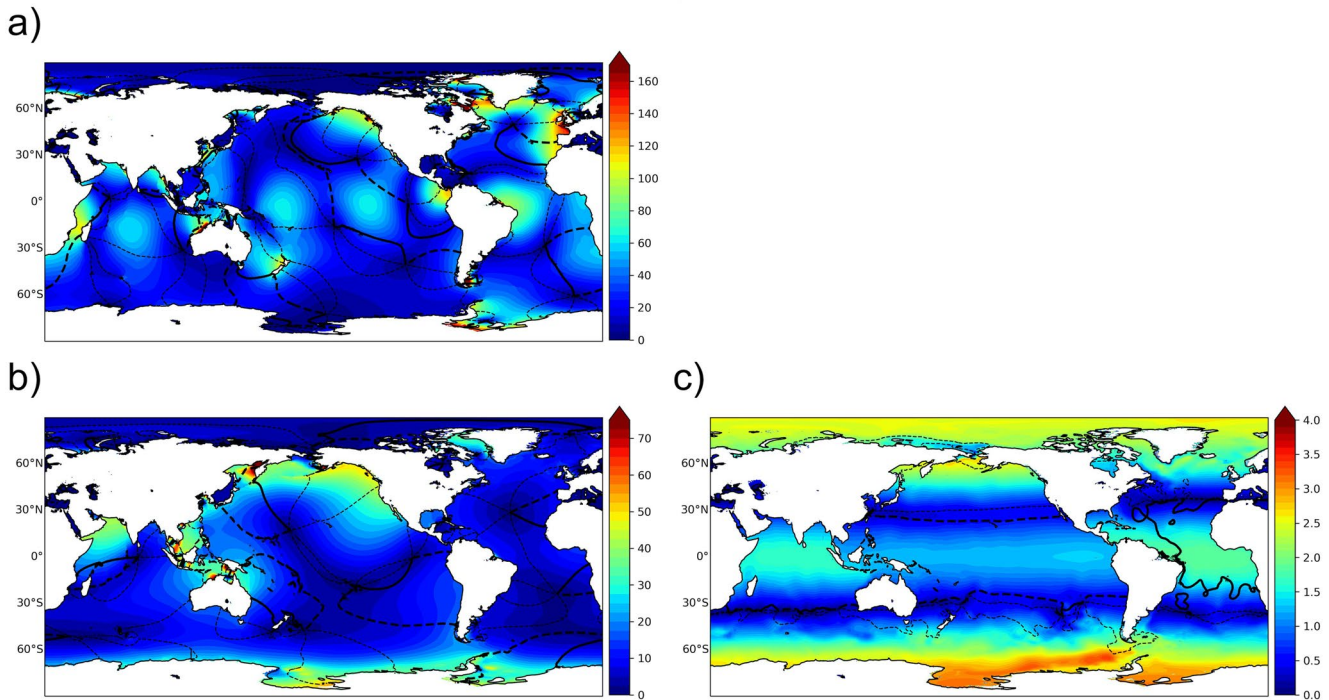
Figure 3. The tidal loads considered in this study shown in terms of the amplitude (pattern) and phase (lines). (a, b, and c) are for the M_2 tide, the K_1 tide and the M_f tide, respectively, in unit cm. The thick line and the thick dashed line represent phase 0° and 60°, respectively. The thin dashed line stands for phases between 120° and 360° with an interval of 60°. The scales are selected to facilitate an overview over the loading patterns, while amplitudes are saturated in several regions (e.g., the Sea of Okhotsk for K_1, the North Atlantic for M_2).

cut-off spherical harmonic degree/order (d/o) 1363 which allows for a 4096 × 2048 Gauss-Legendre grid in the horizontal direction representing a global spatial resolution of ~10 km (~0.089°). This resolution, on the one hand, is far above the resolution of horizontal features of the sediment, lithosphere and mantle structures considered in this study and on the other hand, is rather comparable to the high resolution of the ocean tide model TiME (~0.083°). In the radial coordinate, we are rather flexible and chose resolutions of 1 km above 10 km depth, 2 km between 10 and 50 km, 5 km between 50 and 80 and 10 km between 80 and 670 km. In this way, the structural features of the earth's interior can be resolved accurately. In Section 3.2.1 and Appendix A, we will demonstrate that the LLNs with a cut-off spherical harmonic d/o of 1363 can capture the structural variations in the radial directions of the mantle, lithosphere as well as the sediments of the Earth.

2.3.2. OTD Modeling

By integrating the non-linear shallow water equations (e.g., Pekeris, 1975; Sulzbach et al., 2021; Weis et al., 2008) the ocean tide model TiME predicts the tidal dynamics of the sea surface elevation Z and the tidal transport for the considered individual partial tides M_2, K_1, and M_f. Within the model code, the SAL feedback mechanism to ocean dynamics is slightly different when considering 1D or 3D Earth structures. For 1D elastic/anelastic earth models, the SAL elevation used in shallow water equations is self-consistently included by evaluating

$$\text{SAL} = \frac{\rho_{\text{sw}}}{\rho_E} \sum_{l=1}^{l_{\max}} \sum_{m=-l}^{m=l} \frac{3(1 + k_l - h_l)}{2l + 1} Z_{\text{lm}} Y_{\text{lm}} \tag{2}$$

for each time step, where individual spectral coefficients Z_{lm} of the tidal elevation Z are multiplied with a combination of LLNs, that is, $1 + k_l - h_l$ obtained from the respective earth model. Here, $\rho_{\text{sw}} = 1{,}025$ kg/m³ and $\rho_E = 5{,}510$ kg/m³ are the mean density of seawater and the solid Earth, respectively. In practice, Z is used in Equation 2 to calculate SAL at a given time step, which is then inserted back into the semi-implicit solver to calculate Z at the next time step. In this way, the updated effect of SAL is considered at each time step leading to a self-consistent representation of SAL. For 3D earth models, the SAL elevation used in tidal modeling cannot be obtained by Equation 2 because lateral heterogeneity contradicts the Love number approach representing

the response of a spherically symmetric earth structure. Instead, it is calculated by SAL(3D) = SAL(1D) + [SAL(3D) − SAL(1D)] where SAL(1D) is the SAL elevation for the 1D earth model computed by Equation 2 and [SAL(3D) − SAL(1D)] is the SAL difference between the 3D and 1D earth models which is subject to an initial tidal elevation field and calculated by VILMA-E. As such, SAL(1D) and Z are updated iteratively while [SAL(3D) − SAL(1D)] is treated as a static forcing term in the shallow water equations. This static forcing can be seen as a small perturbation inflicted on the tidal oscillation system that provokes a comparably small response. As we will see later, the smallness of this response renders this first order perturbation treatment sufficient to depict the ocean tidal response to the pure 3D-effect (see Section 3.2).

3. Results and Discussions

3.1. Impact of More Realistic 3D Earth Structures on OTL Displacement and SAL

3.1.1. The Impact of Sediments and Oceanic/Continental Lithosphere

Shown in Figure 4 are the amplitude differences of vertical OTL displacement between models LH-3De and PREM for the M_2, K_1, and M_f OTL. The amplitude differences arise from the impact of more realistic 3D sediments and oceanic/continental lithosphere structures pertaining to LITHO1.0 which is a sum of the pure 1D effect (due to radial structure variations) and the effect of lateral heterogeneity (see Equation 3). Because the ocean tide amplitude decreases with the increasing tidal period (from 12.42 hr for the M_2 tide to 13.66 days for the M_f tide), a decrease in the amplitude difference can be seen, from the order of 1 mm to that of 0.01 mm. In the oceans where PREM underestimates the lithosphere strength, notable amplitude reductions appear and coincide with locations of relatively large tidal amplitudes (compare Figures 3 and 4). In contrast, at the MORs where PREM overestimates the strength, a tiny amplitude enhancement can be observed, with the values being less than 0.3, 0.2, and 0.01 mm for the OTL M_2, K_1, and M_f, respectively. Furthermore, in continental-shelf areas where the continental and oceanic lithosphere and the sediments have a cumulative impact, we see a relatively large amplitude enhancement for all tidal loading, for example, an enhancement of above 2 mm for M_2 in the Bay of Biscay (in the western coast of France) with rather thick sediments. This suggests the dominant impact of sediments and the lower crust, associated with their rather weak structure (Figures 1b and 1d). Be aware that vertical displacements in continental areas, however, are barely affected, except for those in land areas adjacent to OTL with large amplitude, such as the coastal areas of New Zealand, Ryukyu Islands and western Europe shown successively in the lower panel of Figure 4a. In particular, in the southwestern coastal area of England, there is a Global Positioning System (GPS) station in Newlyn where an amplitude change of ∼0.8 mm is predicted for the M_2 load (lower right panel of Figure 4a). This is not a surprise given the fact that shallow Earth structure variations only greatly affect displacements in the near field of loading. In addition, due to the fact that the M_f tide is relatively high in the northern coastal areas of the Eurasian, North American and Antarctic continents where sediments are thick (compare Figure 3c with Figure 1a), a rather evident sediment effect can be identified from the amplitude difference pattern (Figure 4c). In Figure S2 in Supporting Information S1, we present the SAL amplitude differences between LH-3De and PREM. In general, a SAL difference field of similar magnitude can be seen, indicating that the geoid displacement caused by ocean tides are barely affected by variations in elastic moduli.

When the sediment structure in LITHO1.0 is replaced by newSed, we find a similar pattern in the OTL displacement/SAL amplitude difference field with the majority of magnitudes concentrated in the same range (compare Figure S3 in Supporting Information S1 with Figure 4 and Figure S2 in Supporting Information S1). This implies that the sediment impact estimated by LITHO1.0 is reproduceable and thus reliable to some extent. However, since newSed has a weaker sediment structure than LITHO1.0 in most coastal regions (see Section 2), a slightly larger and more widespread displacement/SAL enhancement can be observed for all tidal constituents (compare Figure S3 in Supporting Information S1 with Figure 4 and Figure S2 in Supporting Information S1). Recall that, newSed is made up of densities and velocities that are not consistently inverted for but manually taken from different models, which makes it less consistent than LITHO1.0. Therefore, results based on newSed should be regarded as less reliable. On the other hand, when the 3D lithosphere model WINTERC-G (without sediments) is used instead of LITHO1.0, an amplitude difference pattern that greatly resembles that for LITHO1.0 can be observed for displacement and SAL, but with much greater magnitude, in both shallow and deep water areas (compare Figure S4 in Supporting Information S1 with Figure 4 and Figure S2 in Supporting Information S1). For example, compared to LITHO1.0, WINTERC-G produces ∼1.0 mm less M_2 displacement/SAL in the central Pacific ocean and ∼2 mm less in the Bay of Biscay. This arises from the fact that WINTERC-G consists of a
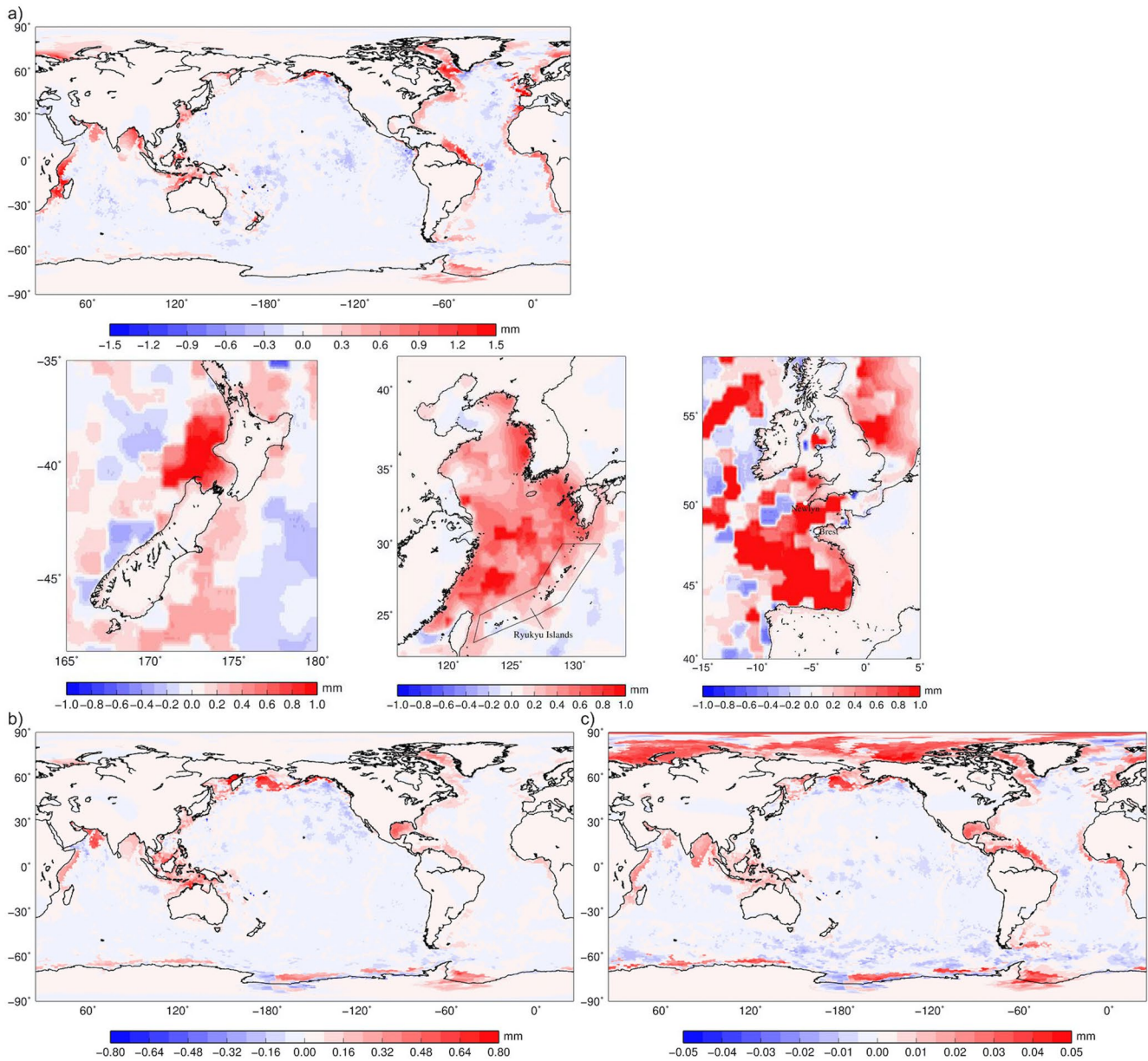
Figure 4. The amplitude difference in vertical ocean tide loading displacement between LH-3De (see Tables 1 and 2 for its definition) and PREM for the M_2 load (a), the K_1 load (b) and the M_f load (c). Subplots in the lower panel of (a), from left to right, show the amplitude difference in coastal areas of New Zealand, Ryukyu islands and western Europe, respectively.

much stronger lithosphere and does not account for sediments (see Section 2). Note that, similar to LITHO1.0, in the Gulf of Mexico and almost all continental shelf regions WINTERC-G produces more displacement/SAL than PREM for all three tidal loading, the M_f load in particular. This is due to a weaker 3D oceanic structure of the lower crust (see the subplot—depth 24 km of Figure S1b in Supporting Information S1) in coastal areas (coinciding with the locations of sediments).

In Table 3, we summarize the peak amplitude differences in vertical displacement and SAL elevation between the abovementioned 3D elastic models and PREM. Combining data of LH-3De, LH-nS-3De, and WG-3De, we conclude that the impact of 3D sediments and lithosphere on the vertical displacement and SAL elevation is in the range of -7.4 to $+5.6$ mm for the M_2 load, -3.1 to $+3.4$ mm for the K_1 load and -0.13 to $+0.08$ mm for the M_f load.

Table 3
The Minimum and Maximum Amplitude Differences of Vertical Ocean Tide Loading (OTL) Displacement (U) and Self-Attraction and Loading (SAL) Elevation Between Different Hybrid Elastic/Anelastic Models (Tables 1 and 2) and PREM for the OTL M_2, K_1, and M_f

	U				
	LH-3De − PREM (mm)	LH-nS-3De − PREM (mm)	WG-3De − PREM (mm)	Lyon-3Dae − PREM (mm)	LH-Lyon-3Dae − PREM (mm)
M_2	−5.4/+3.4	−7.4/+5.6	−2.5/+1.3	−0.4/+1.1	−5.1/+3.9
K_1	−2.4/+1.9	−3.1/+3.4	−1.0/+0.9	−0.3/+1.0	−2.4/+2.6
M_f	−0.096/+0.058	−0.130/+0.080	−0.065/0.020	−0.028/0.042	−0.090/0.086
	SAL				
	LH-3De − PREM (mm)	LH-nS-3De − PREM (mm)	WG-3De − PREM (mm)	Lyon-3Dae − PREM (mm)	LH-Lyon-3Dae − PREM (mm)
M_2	−5.5/+3.4	−7.4/+5.4	−2.5/+1.2	−0.4/+1.1	−5.1/+3.9
K_1	−2.4/+1.9	−3.1/+3.3	−1.0/+0.8	−0.3/+1.0	−2.4/+2.5
M_f	−0.098/+0.059	−0.130/+0.080	−0.065/+0.020	−0.017/+0.042	−0.091/+0.085

3.1.2. The Impact of Anelastic Upper Mantle

In Figure 5, we show the amplitude differences of vertical OTL displacement between Lyon-3Dae and PREM for the M_2, K_1, and M_f loads. The amplitude difference is caused by radial structure variations (the pure 1D effect, see Equation 3) and lateral structure inhomogeneity (the effect of lateral heterogeneity (see Equation 3). It can be
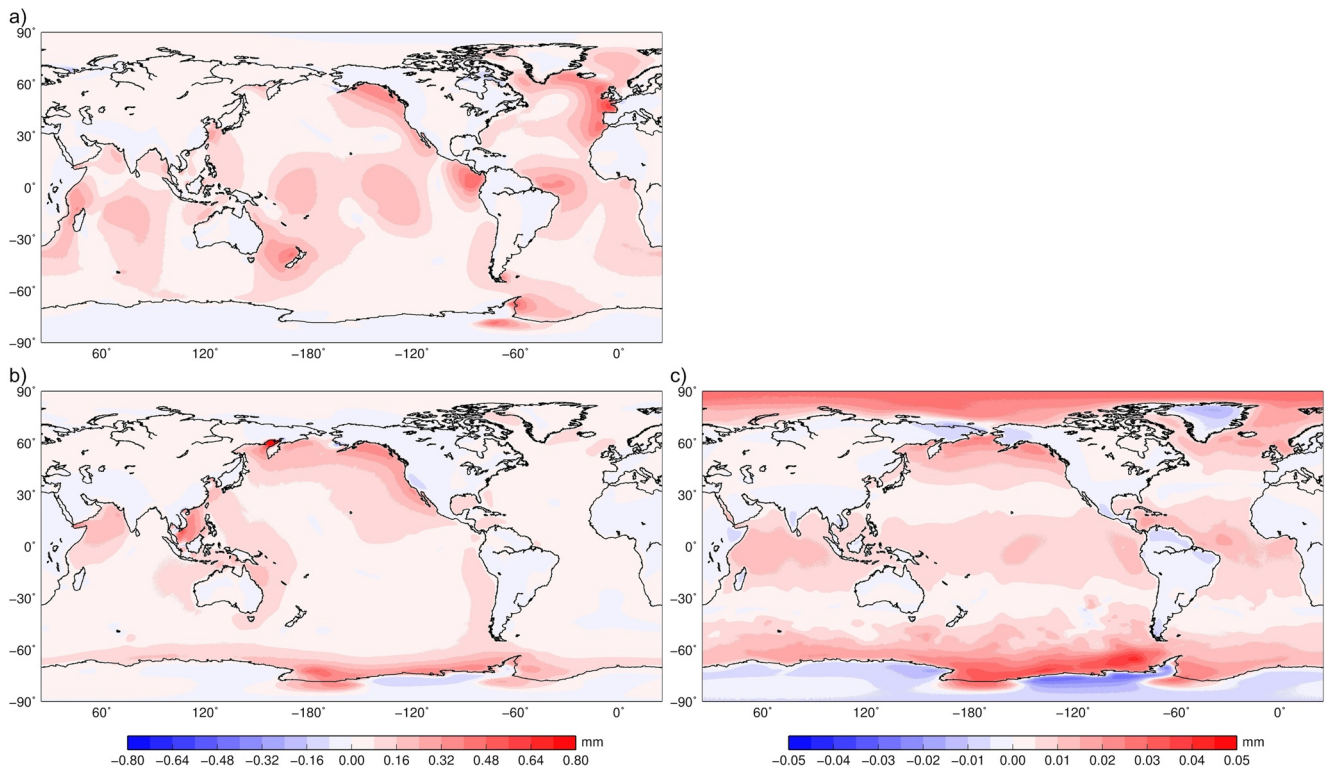

Figure 5. The amplitude difference in vertical ocean tide loading (OTL) displacement between Lyon-3Dae (see Tables 1 and 2 for definition) and PREM for the OTL M_2 (a), K_1 (b) and M_f (c).

seen that, the anelastic upper mantle pertaining to Lyon-3Dae causes a displacement increase for all three tidal loads, most significantly in open ocean areas and coastal areas where tidal amplitudes are large and seismic attenuation is high, which is in agreement with the findings of Huang et al. (2021). For inland continents away from coastal regions, however, displacements decrease, which is consistent with the findings of Experiments 1 and 2 of Huang et al. (2021). In addition, despite of the increase of shear modulus reduction with the increasing tidal period, we see a decrease of the anelastic impact on vertical OTL displacement from the order of 1–0.01 mm, due to the decreasing ocean tide amplitude. Comparing Figure 5 with Figure 4 shows that, in open ocean areas the impact of anelastic mantle is in general opposite to, but slightly larger and more widespread than the impact of sediments and oceanic lithosphere imposed by LITHO1.0; in coastal areas with thick sediments, however, the former effect is evidently smaller than the latter. A similar impact on the SAL elevation can be observed in Figure S5 in Supporting Information S1. The minimum and maximum amplitude differences of U/SAL between Lyon-3Dae and PREM are −0.4/+1.1 mm for the M_2 load, −0.3/+1.0 mm for the K_1 load, −0.028/0.042 mm for the M_f load (Table 3), smaller than but comparable in terms of the order of magnitude to the peak impact of sediments and oceanic lithosphere (compare Table 3 internally).

3.1.3. The Coupled Impact of Sediments, Oceanic Lithosphere and Anelastic Upper Mantle

The previous sections demonstrated that the impact of sediments and oceanic lithosphere could be opposite to or in line with the impact of anelastic upper mantle, therefore, neglecting any of them biases the modeled results. In this section, we study the coupled impact of these earth structures.

As shown previously, the impact of sediments in coastal areas is relatively reliably estimated with newSed and LITHO1.0 generating comparable vertical OTL displacement and SAL, but the impact of oceanic lithosphere is rather uncertain for WINTERC-G producing much smaller displacement that can be more than 1 mm smaller than LITHO1.0 in open ocean areas. Therefore, to study the coupled effect, the selection of an appropriate lithosphere model is essential. We constructed a hybrid earth model called LH-Lyon-3Dae with the sediments and lithosphere structures chosen from LITHO1.0 and the anelastic upper mantle from the Lyon model. The reasons why we used LITHO1.0 instead of WINTERC-G or newSed are as follows: (a) the sediment and oceanic lithosphere structures in LITHO1.0 are jointly and consistently inverted for; (b) WINTERC-G does not contain a sediment structure and so produces extra artificial inconsistency when combined with other sediment structures; (c) the OTL signal of newSed is in general comparable to LITHO1.0, but the elastic moduli of newSed are computed using densities and thickness from newSed and velocities from LITHO1.0, making it less reliable than the elastic moduli of sediments in LITHO1.0.

Figure 6 (left column) shows the amplitude differences of vertical OTL displacement between LH-Lyon-3De and PREM for the M_2, K_1, and M_f tidal loading. It can be seen that, in coastal areas with sediments, the anelastic upper mantle, the sediments and the lower crust impose a constructive impact, creating increased displacement; in most of the open ocean areas, the effects of anelastic upper mantle and the oceanic lithosphere interfere destructively, generating decreased displacement. In particular, we see large displacement enhancements of more than 2 mm in the Bay of Biscay, Celtic Sea and English Channel for the M_2 tide, more than 0.6 mm in the Gulf of Mexico, Bering Sea, Antarctica shelf regions for the K_1 tide, and more than 0.06 mm in the continental shelf regions of Antarctica, Russia and Alaska for the M_f tide. In contrast, in open ocean areas, much smaller displacement enhancement, 0–0.6 mm for the M_2 tide, 0–0.24 mm for the K_1 tide and 0–0.018 mm for the M_f tide can be observed. Due to the relatively large uncertainty in oceanic lithosphere strength revealed from the difference between WINTERC-G and LITHO1.0, we cannot conclude here, that the coupled impact of anelastic upper mantle and oceanic lithosphere are negligible in open ocean areas. The peak coupled impact of sediments, oceanic lithosphere and anelastic upper mantle on displacement revealed by LH-Lyon-3Dae is in the range of −5.1 to +3.9 mm for the M_2 tide, −2.4 to +2.6 mm for the K_1 tide and −0.091 to +0.086 mm for the M_f tide (Table 3). Similar results for SAL are shown in the left column of Figure S6 in Supporting Information S1 and in the lower panel of Table 3.

Figure 6 (right column) shows the relative amplitude difference in vertical OTL displacement between LH-Lyon-3De and PREM. It can be seen that, for the OTL M_2 the relative difference can be above 4% in regions with thick sediments such as the Bay of Biscay, the North Sea, the coastal area of eastern United States, Canada, Russia, India. For the K_1 load, the relative difference can be above 5% in the coastal areas of South America and Greenland. In the Gulf of Mexico, the relative difference is significantly larger, reaching over 15%. For the M_f load, the relative difference is particularly large (above 3%) in the continental-shelf regions of Russia, Alaska,
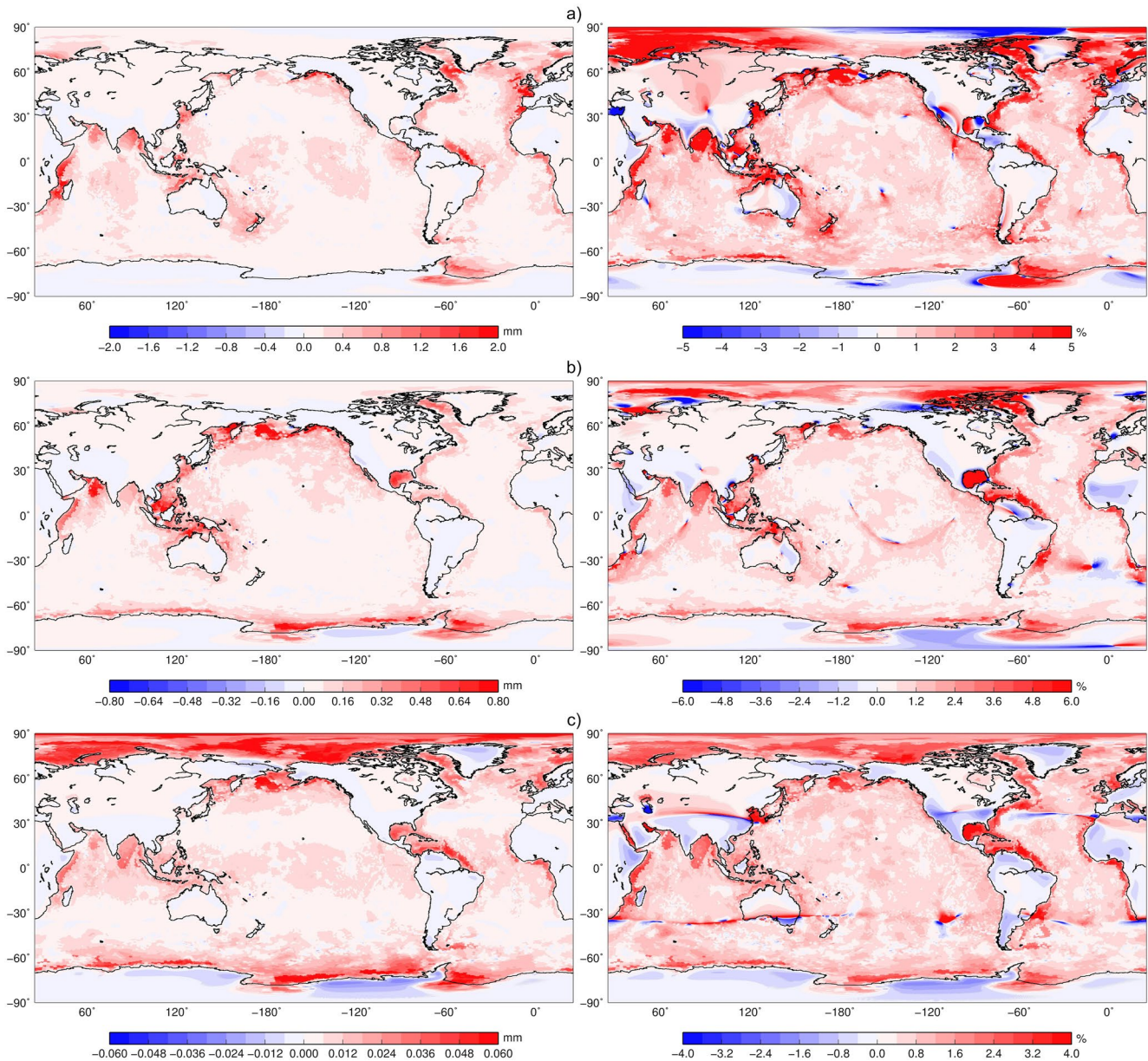
Figure 6. Left panel: the vertical ocean tide loading displacement amplitude difference between LH-Lyon-3De and PREM for the M_2 load (a), the K_1 load (b) and the M_f load (c). Right panel: the same as the left column but for the relative difference.

Antarctica. Again, in the Gulf of Mexico, this difference can be above 5%. Similar results for SAL are shown in the right column of Figure S6 in Supporting Information S1.

The aforementioned amplitude difference in OTL displacement between LH-Lyon-3Dae and PREM arising from structure variations in both radial and lateral directions (Equation 3). To demonstrate the net impact of lateral heterogeneity, we show the amplitude differences between the 3D model LH-Lyon-3Dae and its global mean model (so 1D) LH-Lyon-1Dae in vertical OTL displacement and SAL, respectively, in Figure 7 and Figure S7 in Supporting Information S1. From these figures, it can be observed that if lateral heterogeneities are neglected, displacements are greatly underestimated in coastal regions with sediments and overestimated in most open ocean areas. The underestimation in sedimentary regions for the M_2, K_1, and M_f loads can be larger than 1, 0.4, and 0.03 mm, respectively, and can explain more than 60% of the difference between LH-Lyon-3Dae and PREM.
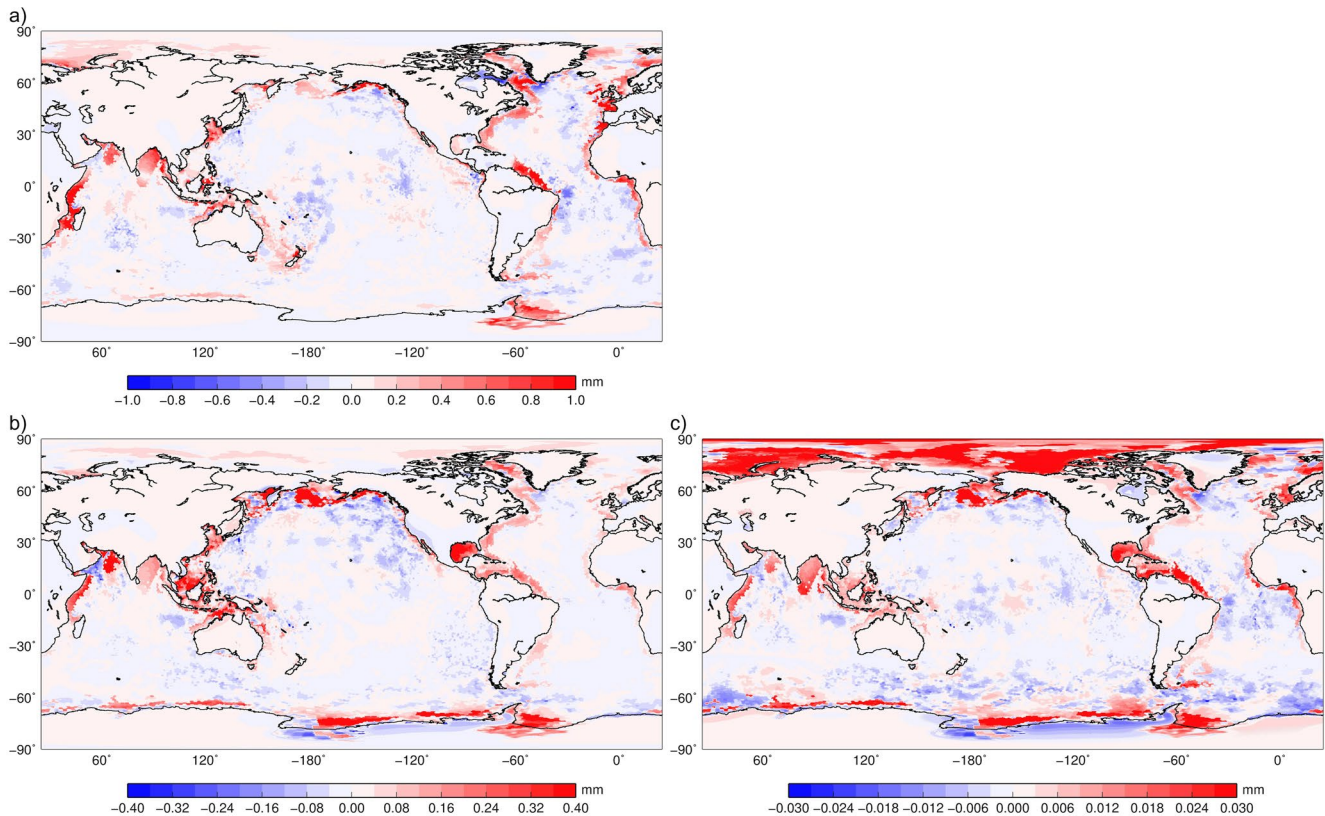
Figure 7. The displacement amplitude difference between the 3D anelastic model LH-Lyon-3Dae and the 1D anelastic model LH-Lyon-1Dae for the M_2 load (a), the K_1 load (b) and the M_f load (c).

3.1.4. Comparison of Modeled OTL Displacements With GNSS Observations

In the previous three Sections 3.1.1–3.1.3, we systematically investigate the impact of sediments, oceanic/continental lithosphere on OTL displacement and show that the combined effect of these structures should be considered instead of an individual effect. A question naturally arises whether this combined impact can be confirmed by observations. Therefore, we turn to looking at vertical OTL displacements modeled by LH-Lyon-3Dae at individual GNSS sites, and compare them to GNSS observations. GNSS stations from western Europe (Bos et al., 2015), East China Sea (Wang et al., 2020), New Zealand (Matviichuk et al., 2021) and Alaska (Martens & Simons, 2020), which amount to 256, 102, 170, and 135, respectively, are included (Table S1). The quality of modeled displacements for LH-Lyon-3Dae was quantified by the vector difference with GNSS estimations, which were independently derived in the above publications. As a comparison, we also calculated the vector difference for displacements predicted by PREM and LH-Lyon-1Dae; results for the RMS of the vector difference are shown in Table 4. It can be seen that in all individual regions except East China Sea, the RMS of the vector difference with GNSS estimations for LH-Lyon-3Dae is approximately 0.1–0.2 mm smaller (precise to 0.1 mm) than that of PREM, and when stations in all regions (663 stations including those from East China Sea) are taken into account, the RMS of the vector difference for LH-Lyon-3Dae is again ∼0.1 mm smaller than that of PREM. This can be regarded as an evidence of the higher overall quality of LH-Lyon-3Dae, and so a confirmation of the cumulative impact of sediments, oceanic/continental lithosphere and anelastic upper mantle. In addition, comparison of the RMS of the vector difference for LH-Lyon-3Dae and LH-Lyon-1Dae shows that the former is ∼0.02–0.05 mm smaller than the latter in all individual regions except East China Sea and the former is 0.02 mm smaller than the latter when all regions are taken into account. This also indicates the higher overall quality of LH-Lyon-3Dae over LH-Lyon-1Dae, supporting the effect of lateral heterogeneity in land areas as shown in Figure 7 (together with the evidence of a better amplitude fit for LH-Lyon-3Dae, see following). Our further calculation of the RMS difference (in phase and amplitude, respectively) between observations and predictions shows that, LH-Lyon-3Dae is slightly worse than LH-Lyon-1Dae and PREM in fitting GNSS-estimated phases at 638 sites (25 sites in western

Table 4
Root-Mean-Square of the Magnitudes of Vector Difference Between Predicted Vertical Ocean Tide Loading Displacements by LH-Lyon-3Dae, LH-Lyon-1Dae and PREM and Those Estimated by GNSS Observations in Western Europe, East China Sea, New Zealand, Alaska and all These Regions

	Western Europe (256 sites, Bos et al., 2015), Center of mass of the solid Earth frame	East China Sea (102 sites, Wang et al., 2020), Center of mass of the whole Earth frame	New Zealand (170 sites, Matviichuk et al., 2021), Center of mass of the whole Earth frame	Alaska (135 sites, Martens and Simons, 2020), Center of mass of the whole Earth frame	All regions (663 sites)
PREM (mm)	3.09	2.98	3.72	3.41	3.31
LH-Lyon-1Dae (mm)	2.99	3.04	3.61	3.36	3.24
LH-Lyon-3Dae (mm)	2.94	3.15	3.57	3.34	3.22

Europe are excluded from the 663 sites because the phase predictions for all the three models are more than 20° away from the observations), with the RMS difference of 9.1°, being 0.1° larger than that of LH-Lyon-1Dae and PREM (9.0°); while LH-Lyon-3Dae has a higher quality in fitting GNSS-estimated amplitudes at the 663 sites, with the RMS difference being 2.4 mm, smaller than the RMS differences for LH-Lyon-1Dae and PREM, being 2.5 and 2.6 mm, respectively. Finally, we acknowledge that the poorer performance of LH-Lyon-3Dae in East China Sea to some extent reveals the artifact of local 3D structures, or on the other hand, the low accuracy of the ocean tide model TiME in such an extended Shelf region. Be reminded that, for readers' reference we include the vertical OTL displacement predictions based on LH-Lyon-3Dae, LH-Lyon-1Dae and PREM as well as the GNSS observations in all 663 GNSS stations in Table S1.

3.2. OTL Feedback on OTD

3.2.1. The Secondary Tide-Generating Potential–The SAL-Difference Potential

We now consider the OTL feedback on OTD with the model LH-Lyon-3Dae and compare it to the dynamics based on PREM. This feedback arises due to the discussed changes in SAL potential that induce a horizontal barotropic acceleration acting on the water masses (e.g., Huang et al., 2021). The altered OTD can thus be treated as the result of a differential SAL potential that we describe as $\Delta\Phi$. In our case, this is the SAL-difference potential between LH-Lyon-3Dae and PREM, that is, $\Delta\Phi = g \cdot (\text{SAL}(\text{LH-Lyon-3Dae})—\text{SAL}(\text{PREM}))$, where g is the surface gravity. Note that, the effect of the difference potential must be considered in interaction with the initially considered tidal dynamics of the 1D-PREM earth model due to nonlinearities of the partial differential equations.

The SAL difference between LH-Lyon-3Dae and PREM is decoupled into two parts, that is,

$$\text{SAL(LH-Lyon-3Dae)} - \text{SAL(PREM)} = [\text{SAL(LH-Lyon-1Dae)} - \text{SAL(PREM)}] + [\text{SAL(LH-Lyon-3Dae)} - \text{SAL(LH-Lyon-1Dae)}] \tag{3}$$

The first term in square-brackets (multiplied by g) on the right-hand side of Equation 3 denotes the principal dynamic potential induced by the difference between the mean structures LH-Lyon-1Dae and PREM. As PREM and LH-Lyon-1Dae are both 1D Earth structures they can be described by two sets of LLNs. Thus this difference potential can be expressed by differences of these LLNs (see Figure A1 and Equation 2). The second difference in square-brackets denotes a static potential arising from lateral heterogeneities in LH-Lyon-3Dae and acting as a correction in OTD modeling. As outlined in Section 2.3.2, "static" indicates that this difference potential is not re-affected by its own impact on OTD (as the first dynamic part does) but treated as a constant. The difference terms in Equation 3 were evaluated up to d/o 1363, and we show in Appendix A why cut-off degree 1363 is necessary and appropriate in our calculations.

To get an impression on the magnitude of the SAL-difference potential ($\Delta\Phi$), or equivalently, the SAL (elevation) difference, we calculate the RMS of the SAL difference between two models by

$$\text{RMS(SAL)} = \sqrt{\frac{1}{2}\left([\text{SAL(m1)} - \text{SAL(m2)}]^2_{\text{in-phase}} + [\text{SAL(m1)} - \text{SAL(m2)}]^2_{\text{quadrature}}\right)} \tag{4}$$

which considers both the in-phase and quadrature components. In Equation 4, m1 and m2 represent models 1 and 2, respectively. Here, we consider three model pairs, that is, LH-Lyon-3Dae and LH-Lyon-1Dae (to show the pure effect of lateral inhomogeneity, or the pure 3D-effect), LH-Lyon-1Dae and PREM (to show the effect of anelasticity and changes in elasticity, or the mean 1D-effect), LH-Lyon-3Dae and PREM (to show the full effect), and present results in Figure 8.

Inspection of Figure 8 shows that, for all three tidal constituents the SAL difference (potential) between the 3D and 1D anelastic models are comparable and even larger than the difference between the 1D anelastic model and PREM in coastal regions with sediments, but are less widespread and less continuous in open ocean areas. The SAL difference pattern between LH-Lyon-1Dae and PREM resembles more the pattern of OTL forcing while the difference pattern between LH-Lyon-3Dae and LH-Lyon-1Dae reveals more the horizontal structural variations of the solid Earth. For example, due to the existence of thick sediments, the SAL differences between LH-Lyon-3Dae and LH-Lyon-1Dae are particularly large in the western coastal regions of Africa and America for the M_2 tide, in the Gulf of Mexico and Bering Sea for the K_1 tide, and in the northern coastal regions of Russia and Alaska for the M_f tide. In terms of the SAL difference between LH-Lyon-3Dae and PREM, most of them are in the range of 0–2.0 mm for the M_2 tide, 0–1.0 mm for the K_1 tide and 0–0.05 mm for the M_f tide. Exceptionally large differences are found to be more than 2 mm in the Bay of Biscay for the M_2 tide, above 1 mm in the Sea of Okhotsk for the K_1 tide and over 0.05 mm in the coastal regions of Alaska for the M_f tide.

3.2.2. The Tide Generated by the SAL-Difference Potential

Shown in Figures 9a–9c are the tides generated by the SAL-difference potential $g \cdot$ (SAL(LH-Lyon-3Dae)—SAL(LH-Lyon-1Dae)), $g \cdot$ (SAL(LH-Lyon-1Dae)—SAL(PREM)) and $g \cdot$ (SAL(LH-Lyon-3Dae)—SAL(PREM)), respectively. Inspection of Figure 9 shows that the impact of the respective differential SAL-forcing on OTD depicted as the RMS of the induced sea surface variations, RMS(Z), differs strongly, depending on the respective tidal frequency and whether the pure 3D-effect (SAL(LH-Lyon-3Dae)—(SAL(LH-Lyon-1Dae)), the mean 1D-effect (SAL(LH-Lyon-1Dae)—SAL(PREM)) or both effects are considered. The global RMS(Z) does not coincide with the RMS(SAL) (compare Figure 9 with Figure 8), that is, the ocean response does not agree with the forcing potential, as one would expect for equilibrium tidal dynamics. The induced OTD of the differential potential should be pictured to be mediated by means of so-called *oceanic normal modes* (e.g., Müller, 2008) where the ocean response sensitively depends on the frequency, global characteristics of the OTD and the specific pattern (in terms of phase and amplitude) of the exciting potential. When OTD are excited near-resonantly, the ocean response will show the pronounced long-range correlated characteristics of those normal modes, and not the spatial characteristics of the initial forcing potential (here: the differential SAL-forcing).

In accordance with the findings of Shihora et al. (2022), the impact of the differential SAL-forcing is weakest for the long-period M_f tide (period ∼ 14 days), as the ocean tides at the M_f period are far from resonance and generally quite close to a pure equilibrium response (as for solid Earth body tides). The effect is even more pronounced for the pure 3D-effect, where RMS(Z) is very similar to RMS(SAL) (compare Figure 9c with Figure 8c), as the characteristic scale of the SAL-potential is very short, thus further reducing resonance with globally interconnected normal modes. In particular, the sediment signal in the SAL-potential is reproduced well in RMS(Z) in the coastal areas of Antarctica, Russia and Alaska. As the 1D effect depicts longer wavelength it is coupled more strongly to the large-scale characteristics of the M_f tide which explains the slight amplification of the SAL-forcing-amplitude in the OTD (compare Figure 8c with Figure 9c).

The ocean feedback changes when investigating the diurnal K_1 tide, where the SAL differential forcing between LH-Lyon-1Dae and PREM couples more resonantly to a number of ocean normal modes. Therefore, the OTD not only shows the characteristics of a few prominent large-scale features but is also amplified with respect to the differential forcing amplitude, for example, approximately by a factor of 2 in the North Pacific (compare Figure 9b with Figure 8b). The same is true for the 3D effect, where some features of the SAL forcing can still be identified, for example, the SAL forcing induced by sediments in the coastal areas of Pakistan (compare Figure 9b with Figure 1a).

It is well known that semidiurnal tides are highly resonant at modern bathymetric conditions (e.g., Müller, 2008; Platzman et al., 1981; Pugh & Woodworth, 2014). Thus, it is not surprising that the M₂-response pattern is even more dominated by a few large-scale features dictated by a number of normal modes (e.g., the North Atlantic amphidromic system) and further strongly elevated with respect to the initial SAL-forcing amplitude (locally up to a factor of 4) (compare Figure 9a with Figure 8a). Also the pure 3D-effect couples more strongly to the oceanic
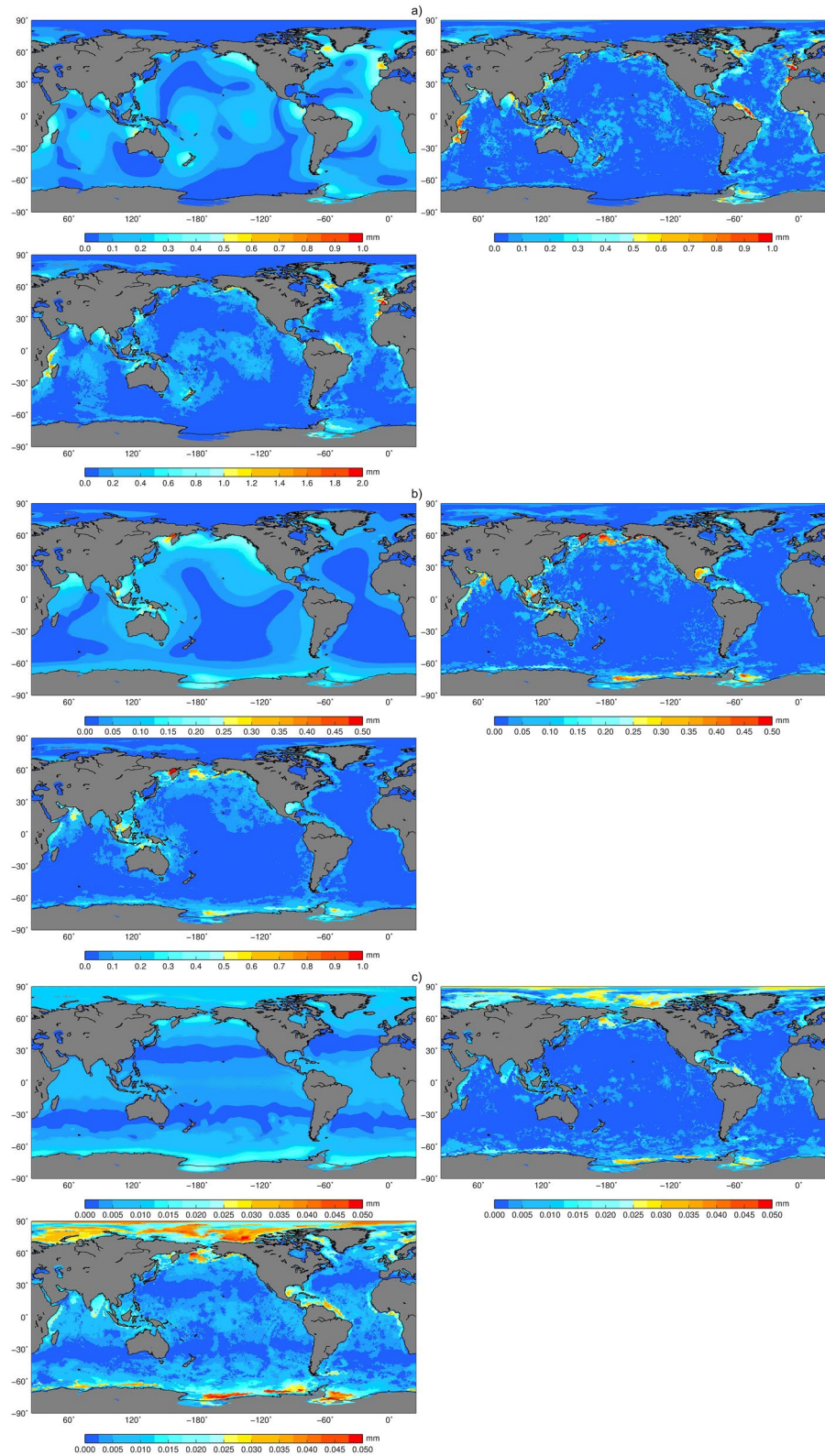
Figure 8. The root-mean-square of the self-attraction and loading difference between LH-Lyon-1Dae and PREM (upper left), LH-Lyon-3Dae and LH-Lyon-1Dae (upper right), and LH-Lyon-3Dae and PREM (lower left) in (a) for the M_2 tide, in (b) for the K_1 tide and in (c) for the M_f tide.
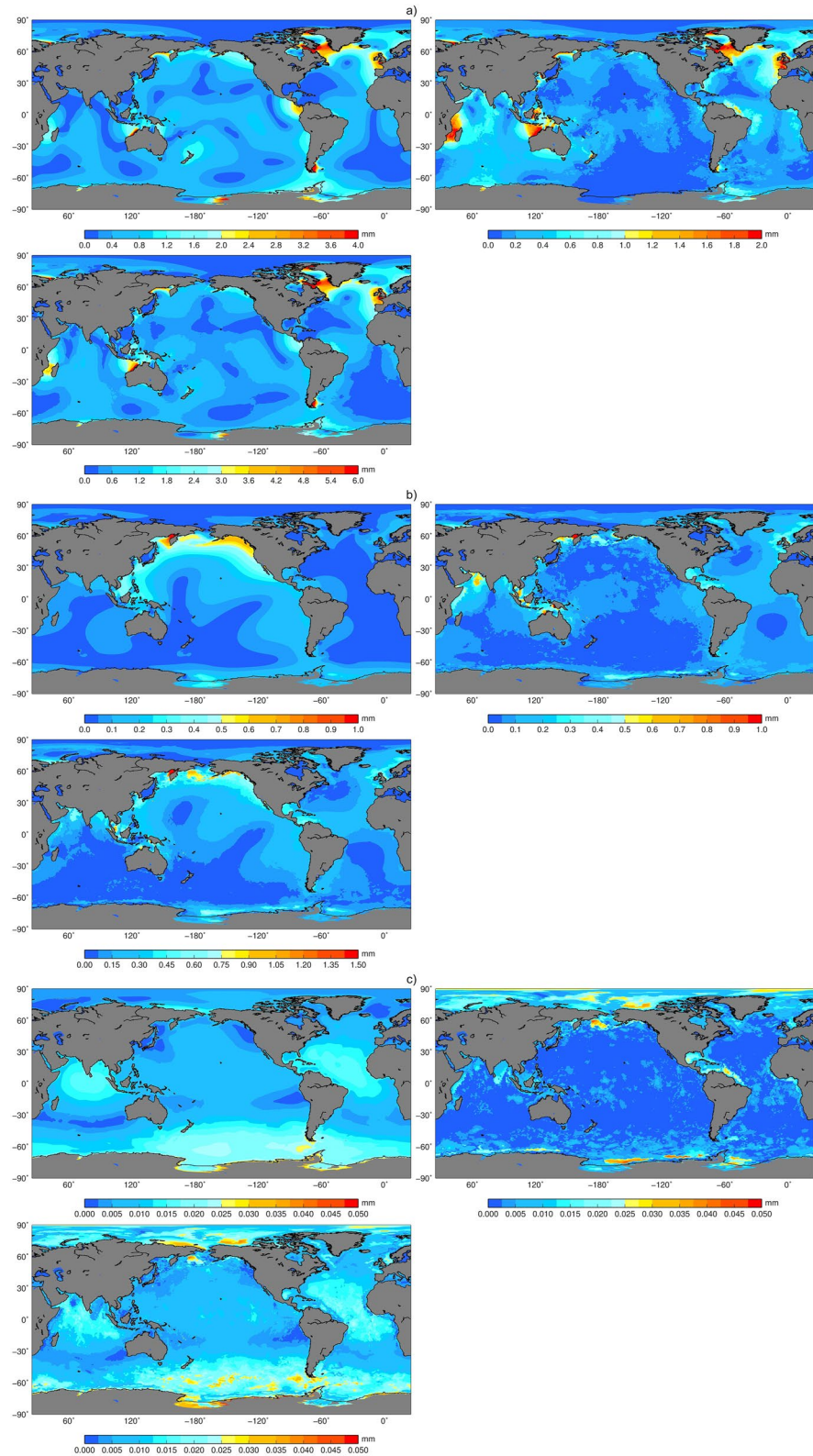
Figure 9. The RMS of tide (Z) difference between LH-Lyon-1Dae and PREM (upper left), LH-Lyon-3Dae and LH-Lyon-1Dae (upper right), and LH-Lyon-3Dae and PREM (lower left). (a, b, and c) show the RMS for the tides M_2, K_1, and M_f, respectively.

eigenmodes as semidiurnal amphidromic systems take place on shorter spatial scales that are thus closer to the scales of the pure 3D-effect patterns. The M_2-results can be seen in the light of the results of Huang et al. (2021) where similar behavior was reported.

The results for the full effect (SAL(LH-Lyon-3Dae)—SAL(PREM)) can be seen as the superposition of the discussed pure 1D and 3D effects that can be constructive or destructive depending on the local phase difference of both effects. The scales for the oceanic response increase, depending on the individual resonance strength as discussed above. For example, with respect to the M_2 tide, the generated tide is mostly in the range of 0–6 mm and therefore much larger than the range of SAL difference (0–2.0 mm) between LH-Lyon-3Dae and PREM (see Figure 9a).

With respect to the validation of the employed model with real oceanographic data (e.g., tide gauge or satellite altimetric data), the small amplitude of the discussed effect in the range of only a few millimeters renders it difficult to quantify a possible accuracy improvement of the introduced tidal model, that is, the RMS deviation from an ensemble of tide gauge stations for M_2/K_1 amounts to 48.3/13.2 mm (Sulzbach et al., 2021), making a mean effect of about 2.0/0.5 mm hard to detect. However, given the millimeter accuracy level of modern data-constrained tidal models (e.g., Stammer et al., 2014), the impact of sediments, oceanic lithosphere and anelastic upper mantle on geocentric tide (ocean tide + vertical displacement) should be regarded as relevant, as both are measured in combination by satellite altimetry.

4. Conclusion

Using structural models LITHO1.0, WINTERC-G, newSed and Lyon, we studied the impact of sediments, oceanic and continental lithosphere and anelastic upper mantle on OTL displacement and SAL, and on OTD. In open ocean areas, we consider only oceanic lithosphere and anelastic upper mantle because the sediment thickness is rather small (less than 500 m). In coastal regions, we additionally considered sediments and find that the weak sediment and oceanic lithosphere structures significantly increase the vertical OTL-induced displacements by up to 5.6, 3.4, and 0.1 mm, respectively for the M_2, K_1, and M_f loads with respect to PREM. We also note that the sediment models LITHO1.0 and newSed produce comparable displacements while the lithosphere models LITHO1.0 and WINTERC-G show a wide spread due to significant deviations in the lithospheric strength. On the other hand, it is found that the 3D anelastic upper mantle structure increases the OTL displacement by up to 1.1, 1.0, and 0.04 mm, respectively for the M_2, K_1, and M_f loads. In addition and quite importantly, we demonstrate that a high (global) horizontal resolution of ~10 km or 0.089° (corresponding to a maximum spherical harmonic degree and order 1363) is necessary and appropriate in capturing the deformational effects of sediments, oceanic lithosphere and anelastic upper mantle.

By looking at the global distribution of the individual effects of the lithosphere (with sediments) and upper mantle structures, we found that these two effects can be constructive or destructive; as such, solid earth models neglecting any of them will produce biased OTL displacement predictions. Therefore, we constructed the more realistic 3D hybrid earth model LH-Lyon-3Dae by combining LITHO1.0 for the lithosphere and sediments and the Lyon model for the anelastic mantle to quantify the coupled impact on OTL. We find that, compared to PREM, this more realistic 3D model produces maximum enhancements in OTL displacement of 3.9, 2.6 and 0.086 mm for the OTL M_2, K_1, and M_f, respectively, and a relative enhancement of over 4%, 5% and 3%, separately in coastal regions with thick sediments. In comparison with OTL observations in 663 GNSS stations from western Europe, East China Sea, New Zealand and Alaska, LH-Lyon-3Dae predicted vertical displacements show a RMS of the vector difference of approximately 0.1 mm smaller and an amplitude RMS agreement of 0.2 mm better than PREM, an indication of the higher accuracy of LH-Lyon-3Dae, and so a confirmation of the coupled impact of sediments, oceanic/continental lithosphere and anelastic upper mantle. The effect of lateral heterogeneity is also supported by GNSS observations, with the RMS of the vector and amplitude differences of LH-Lyon-3Dae being 0.02 and 0.1 mm smaller than those of LH-Lyon-1Dae. Furthermore, as relativistic geodesy using fiber-linked optical clocks will be able to improve observational accuracy of tides by providing us with a new type of observation data (e.g., Tanaka and Katori, 2021), accounting for the effect of 3D Earth structures will be more important.

Considering the effect of the Earth's structural features on OTD, we find the impact of 3D sediments, lithosphere and anelastic upper mantle shows larger wavelength and changes patterns with respect to the changes in SAL elevation. Results based on the hybrid earth structure LH-Lyon-3Dae show that at the M_2 and K_1 frequencies, this

impact is concentrated in the ranges 0–6 mm and 0–1.5 mm, respectively, which is considerably larger than the impact on SAL (concentrated in the ranges 0–2 mm and 0–1.0 mm, respectively). This amplification is typical for near-resonant ocean tides. At the M_f frequency, the impact on OTD and that on SAL are similar though, with the majority in the range of 0–0.05 mm. This is due to the fact that M_f is not close to resonance and much closer to hydrostatic equilibrium. While the accuracy level of the employed data-unconstrained ocean tide model TiME is not sufficient to confirm an improvement by considering the 3D earth structure with respect to geodetic data, this situation might change in the future. On the other hand, the impact might be important for ocean tide models that are constrained by satellite altimetry. Given the millimeter accuracy level of modern data-constrained tidal models (e.g., Stammer et al., 2014), accounting for sediments, oceanic and continental lithosphere and anelastic upper mantle in OTD modeling can be beneficial. In addition, due to the relatively large uncertainty in the strength of oceanic lithosphere revealed by comparing WINTERC-G with LITHO1. O, resolving the more accurate effect of oceanic lithosphere on OTD requires further studies.

Appendix A: Why Are LLNs Evaluated to Degree/Order 1363 Able to Resolve the Structural Deviation of LH-Lyon-1Dae From PREM ?

In computing SAL(LH-Lyon-1Dae)—SAL(PREM) or U (LH-Lyon-1Dae)—U(PREM) (U stands for the vertical OTL displacement) [for example, with Equation 2 for SAL and the numerator of Equation 2 replaced by $3h_l$ for U], it is vitally important that the sum and the LLNs are evaluated to an appropriate maximum degree l_{max} such that, on the one hand, the computational cost is affordable and, on the other hand, the LLNs can capture structural differences between the two earth models and sufficiently include the SAL effect on OTD. Huang et al. (2021) showed that anelasticity in the upper mantle mainly affects the LLNs between degrees 4 and 400, but the LLNs should be evaluated to 1024 to include the SAL feedback on OTD in the shallow water areas. Here, we evaluate LLNs up to 1363 and we will illustrate in the following why 1363 is able to capture the structural differences between LH-Lyon-1Dae and PREM.

Shown in Figure A1a is the shear modulus difference in the upper mantle, lithosphere and the sediment layer between LH-Lyon-1Dae and PREM, and in Figure A1b is the difference in LLNs for degrees 0 to 1363 for all three considered tidal frequencies (M_2, K_1, and M_f). It can be observed that, differences in h are identical for all tidal frequencies for degrees above ∼220, but clearly different at respective tidal frequencies for degrees between 4 and ∼220 (Figure A1b). Inspection of Figure A1a shows that, the former is related to the identical shear modulus difference at these three tidal frequencies in the lithosphere and sediments (at radii 6,291 – 6,371 km) between LH-Lyon-1Dae and PREM, while the latter is related to the different shear modulus reductions in the upper mantle (at radii 5,726 – 6,291 km) of LH-Lyon-1Dae at different tidal frequencies. A detailed look shows that, for all tidal frequencies, negative differences in h appear in two degree bands, that is, [4, ∼100] and [∼1309, 1363] (Figure A1b). The former relatively long-wave-length h reveals the dominant impact of anelasticity embedded in the upper mantle as well as the influence of the weak lower crust at radii ∼6,320–6,344 km of LH-Lyon-1Dae (Figure A1a). The latter relatively short-wave-length h reflects the influence of the weak oceanic uppermost crust and sediments at water depths (∼0–5 km) of LH-Lyon-1Dae (Figure A1a). In contrast, a significant positive deviation can be observed for degrees ∼120 to 1309, which is apparently related to the impact of the strong oceanic upper crust included at radii 6,344–6,366 km of LH-Lyon-1Dae. Be also noted that, the anelastic impact on the Love number h are larger for lower tidal frequencies as M_f, associated with the longer relaxation time of the upper mantle subject to longer-period OTL forcing, while the Love number k experiences much smaller deviations than h, indicating the lower sensitivity of k to perturbations in elastic moduli. To sum up, the LLNs up to d/o 1363 can already capture structural differences between LH-Lyon-1Dae and PREM in the upper mantle, lithosphere as well as the sediment layer.
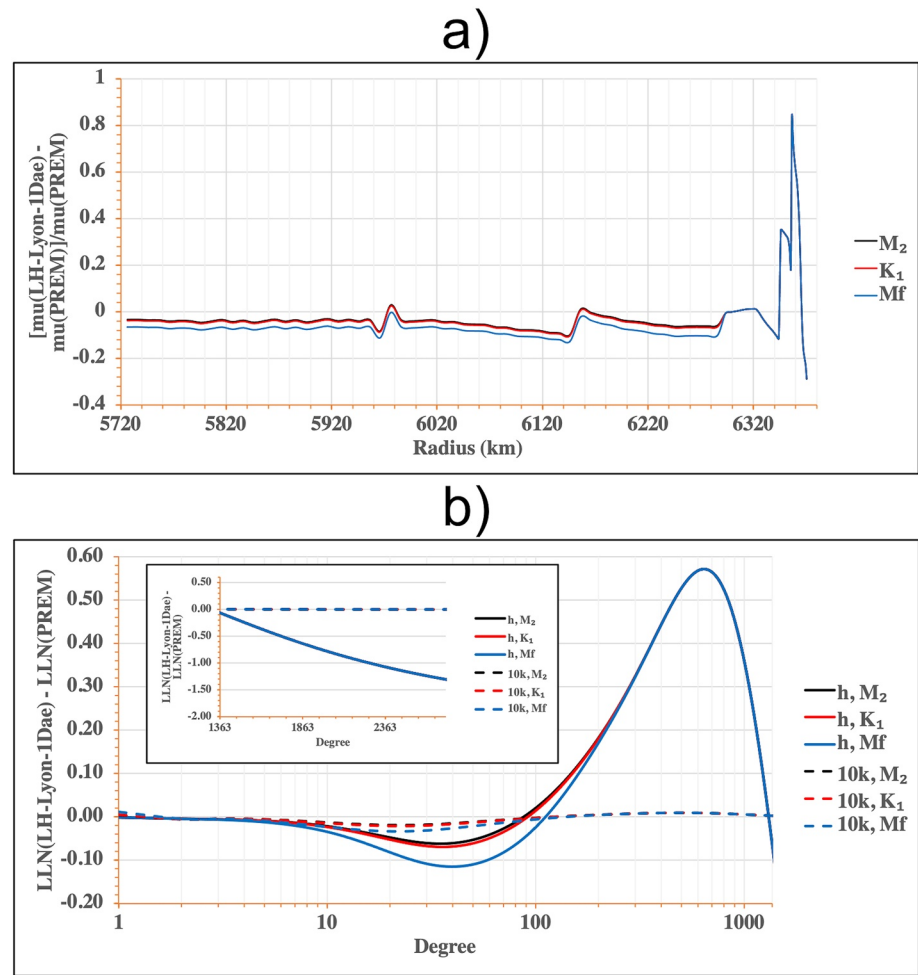
Figure A1. (a) The radial variation of the shear modulus (mu) in LH-Lyon-1Dae with respect to PREM at the tidal frequencies of M_2, K_1, and M_f. (b) The LLNs difference between LH-Lyon-1Dae and PREM at the listed frequencies for degrees 0 to 2728 (10k means the Love number k multiplied by a factor of 10).

To estimate the effect of LLNs of degrees higher than 1363, we also computed the vertical OTL displacement and SAL with a cut-off d/o 2728 for LH-Lyon-1Dae and PREM, as well as the corresponding amplitude differences between LH-Lyon-1Dae and PREM. Results are shown in Tables A1 and A2. Inspection of Tables A1 and A2 shows that, when the maximum d/o increases from 1363 to 2728, the peak (minimum and maximum) amplitude differences change slightly by less than 0.1 mm for all OTL (M_2, K_1, and M_f) considered here (Table A1), and the peak change in amplitude difference is less than 0.2 mm (Table A2). Considering the 0.2–0.4 mm accuracy level of GPS-estimated OTL displacement (Penna et al., 2015), these changes can be regarded as minimal. We finally remark that, although the difference in LLNs becomes larger for degrees higher than 1363 (the small inside plot of Figure A1b), the effect of these LLNs on the amplitude difference is strongly suppressed by the relatively small magnitudes of the factor $1/(2l + 1)$ and the load coefficients Z_{lm} (see Equation 2), less than (or equal to) 10^{-4} and 10^{-5} m, respectively. Therefore, degrees >1363 get a rather small weight in the final evaluation and can be neglected. Finally, we acknowledge that for specific load deformations in the vicinity of strong structural changes and at small-scale load changes, higher degrees are required in deriving appropriate Green's functions (e.g., Chen et al., 2018; Farrell, 1972).

Table A1

The Maximum Positive and Negative Amplitude Differences of Vertical OTL Displacement (U) (Bolded) and SAL Elevation (Not Bolded) Between LH-Lyon-1Dae and PREM for the Two Different Cut-Off Spherical Harmonic Degrees/Orders, That Is, 1363 and 2728

	U, SAL		
	M2	K1	Mf
1363	**−0.3898/+1.1735,**	**−0.2373/+0.9571,**	**−0.0127/+0.0318,**
	−0.3515/+0.9075	−0.2981/+0.7700	−0.0104/+0.0301
2728	**−0.4105/+1.1287,**	**−0.2944/+0.9481,**	**−0.0126/+0.0318,**
	−0.4248/+0.9155	−0.3531/+0.6875	−0.0114/+0.0280

Table A2

The Range of Change in Amplitude Differences of Vertical OTL Displacement (U) (Bolded) and SAL Elevation (Not Bolded) Between LH-Lyon-1Dae and PREM When the Cut-Off Spherical Harmonic Degree/Order Is Increased From 1363 to 2728

	U, SAL		
	M_2	K_1	M_f
2728–1363	**[−0.1664, 0.2215],**	**[−0.1191, +0.0797],**	**[−0.0031, +0.0020],**
	[−0.1731, 0.1165]	[−0.1142, +0.0435]	[−0.0040, +0.0020]

Data Availability Statement

The earth models are available on request to the corresponding author of the paper where the model is published. The modeled displacement data for PREM, LH-Lyon-1Dae and LH-Lyon-3Dae as well as the corresponding GNSS observations in 663 stations are provided in the Supporting Information S1, while more numerical data-sets of displacement, self-attraction and loading and ocean tides for PREM, LH-Lyon-1Dae and LH-Lyon-3Dae in the center of figure frame are being published in GFZ data services (https://dataservices.gfz-potsdam.de/panmetaworks/review/bc5fbc8272ce1fc6cfc7ac2769d3ea2970cb27984a2edb54a5eab329e52015b7/).

References

Adenis, A., Debayle, E., & Ricard, Y. (2017). Attenuation tomography of the upper mantle. *Geophysical Research Letters*, *44*(15), 7715–7724. https://doi.org/10.1002/2017gl073751

Afonso, J. C., Salajegheh, F., Szwillus, W., Ebbing, J., & Gaina, C. (2019). A global reference model of the lithosphere and upper mantle from joint inversion and analysis of multiple data sets. *Geophysical Journal International*, *217*(3), 1602–1628. https://doi.org/10.1093/gji/ggz094

Anderson, D. L., & Minster, J. B. (1979). The frequency dependence of Q in the Earth and implications for mantle rheology and Chandler wobble. *Geophysical Journal International*, *58*(2), 431–440. https://doi.org/10.1111/j.1365-246x.1979.tb01033.x

Artemieva, I. (2011). *Lithosphere: An interdisciplinary approach*. Cambridge University Press.

Bagge, M., Klemann, V., Steinberger, B., Latinović, M., & Thomas, M. (2021). Glacial-isostatic adjustment models using geodynamically constrained 3D Earth structures. *Geochemistry, Geophysics, Geosystems*, *22*(11), e2021GC009853. https://doi.org/10.1029/2021gc009853

Benjamin, D., Wahr, J., Ray, R. D., Egbert, G. D., & Desai, S. D. (2006). Constraints on mantle anelasticity from geodetic observations, and implications for the J 2 anomaly. *Geophysical Journal International*, *165*(1), 3–16. https://doi.org/10.1111/j.1365-246x.2006.02915.x

Bos, M. S., Penna, N. T., Baker, T. F., & Clarke, P. J. (2015). Ocean tide loading displacements in Western Europe: 2. GPS-observed anelastic dispersion in the asthenosphere. *Journal of Geophysical Research: Solid Earth*, *120*(9), 6540–6557. https://doi.org/10.1002/2015jb011884

Chen, J. Y., Pan, E., & Bevis, M. (2018). Accurate computation of the elastic load Love numbers to high spectral degree for a finely layered, transversely isotropic and self-gravitating Earth. *Geophysical Journal International*, *212*(2), 827–838.

Dalca, A. V., Ferrier, K. L., Mitrovica, J. X., Perron, J. T., Milne, G. A., & Creveling, J. R. (2013). On postglacial sea level—III. Incorporating sediment redistribution. *Geophysical Journal International*, *194*(1), 45–60. https://doi.org/10.1093/gji/ggt089

Debayle, E., Bodin, T., Durand, S., & Ricard, Y. (2020). Seismic evidence for partial melt below tectonic plates. *Nature*, *586*(7830), 555–559. https://doi.org/10.1038/s41586-020-2809-4

Dill, R., Klemann, V., Martinec, Z., & Tesauro, M. (2015). Applying local Green's functions to study the influence of the crustal structure on hydrological loading displacements. *Journal of Geodynamics*, *88*, 14–22. https://doi.org/10.1016/j.jog.2015.04.005

Divins, D. L. (2003). *Total sediment thickness of the world's oceans & marginal seas*. National Oceanic and Atmospheric Administration National Geophysical Data Center.

Dziewonski, A. M., & Anderson, D. L. (1981). Preliminary reference Earth model. *Physics of the Earth and Planetary Interiors*, *25*(4), 297–356. https://doi.org/10.1016/0031-9201(81)90046-7

Farrell, W. E. (1972). Deformation of the Earth by surface loads. *Reviews of Geophysics*, *10*(3), 761–797. https://doi.org/10.1029/rg010i003p00761

Fullea, J., Lebedev, S., Martinec, Z., & Celli, N. L. (2021). WINTERC-G: Mapping the upper mantle thermochemical heterogeneity from coupled geophysical–petrological inversion of seismic waveforms, heat flow, surface elevation and gravity satellite data. *Geophysical Journal International*, *226*(1), 146–191. https://doi.org/10.1093/gji/ggab094

Haeger, C., Kaban, M. K., Tesauro, M., Petrunin, A. G., & Mooney, W. D. (2019). 3-D density, thermal, and compositional model of the Antarctic lithosphere and implications for its evolution. *Geochemistry, Geophysics, Geosystems*, *20*(2), 688–707. https://doi.org/10.1029/2018gc008033

Hartmann, T., & Wenzel, H. G. (1995). Catalogue HW95 on the tide generating potential. *Marées terrestres (Bruxelles)*, *123*, 9278–9301.

Huang, P., Sulzbach, R. L., Tanaka, Y., Klemann, V., Dobslaw, H., Martinec, Z., & Thomas, M. (2021). Anelasticity and lateral heterogeneities in Earth's upper mantle: Impact on surface displacements, self-attraction and loading, and ocean tide dynamics. *Journal of Geophysical Research: Solid Earth*, *126*(9), e2021JB022332. https://doi.org/10.1029/2021jb022332

Ivins, E. R., Caron, L., Adhikari, S., Larour, E., & Scheinert, M. (2020). A linear viscoelasticity for decadal to centennial time scale mantle deformation. *Reports on Progress in Physics*, *83*(10), 106801. https://doi.org/10.1088/1361-6633/aba346

Jackson, I., Faul, U. H., Fitz Gerald, J. D., & Tan, B. H. (2004). Shear wave attenuation and dispersion in melt-bearing olivine polycrystals: 1. Specimen fabrication and mechanical testing. *Journal of Geophysical Research*, *109*(B6), B06201. https://doi.org/10.1029/2003jb002406

Jackson, I., Fitz Gerald, J. D., Faul, U. H., & Tan, B. H. (2002). Grain-size-sensitive seismic wave attenuation in polycrystalline olivine. *Journal of Geophysical Research*, *107*(B12), ECV5-1–ECV5-16. https://doi.org/10.1029/2001jb001225

Kaban, M. K., Stolk, W., Tesauro, M., El Khrepy, S., Al-Arifi, N., Beekman, F., & Cloetingh, S. A. (2016). 3D density model of the upper mantle of Asia based on inversion of gravity and seismic tomography data. *Geochemistry, Geophysics, Geosystems*, *17*(11), 4457–4477. https://doi.org/10.1002/2016gc006458

Kaban, M. K., Tesauro, M., & Cloetingh, S. A. P. L. (2010). An integrated gravity model for Europe's crust and upper mantle. *Earth and Planetary Science Letters*, *296*(3–4), 195–209. https://doi.org/10.1016/j.epsl.2010.04.041

Karaoğlu, H., & Romanowicz, B. (2018). Inferring global upper-mantle shear attenuation structure by waveform tomography using the spectral element method. *Geophysical Journal International*, *213*(3), 1536–1558. https://doi.org/10.1093/gji/ggy030

Kennett, B. L., Engdahl, E. R., & Buland, R. (1995). Constraints on seismic velocities in the Earth from traveltimes. *Geophysical Journal International*, *122*(1), 108–124. https://doi.org/10.1111/j.1365-246x.1995.tb03540.x

Klemann, V., Martinec, Z., & Ivins, E. R. (2008). Glacial isostasy and plate motion. *Journal of Geodynamics*, *46*(3–5), 95–103. https://doi.org/10.1016/j.jog.2008.04.005

Kustowski, B., Ekström, G., & Dziewoński, A. M. (2008). The shear-wave velocity structure in the upper mantle beneath Eurasia. *Geophysical Journal International*, *174*(3), 978–992. https://doi.org/10.1111/j.1365-246x.2008.03865.x

Laske, G., & Masters, G. (1997). A global digital map of sediment thickness. *Eos, Transactions, American Geophysical Union*, *78*, F483.

Laske, G., Masters, G., Ma, Z., & Pasyanos, M. (2013). Update on CRUST1. 0—A 1-degree global model of Earth's crust. *Geophysical Research Abstracts*, *15*, 2658.

Lyard, F. H., Allain, D. J., Cancet, M., Carrère, L., & Picot, N. (2021). FES2014 global ocean tide atlas: Design and performance. *Ocean Science*, *17*(3), 615–649. https://doi.org/10.5194/os-17-615-2021

Martens, H. R., Rivera, L., Simons, M., & Ito, T. (2016). The sensitivity of surface mass loading displacement response to perturbations in the elastic structure of the crust and mantle. *Journal of Geophysical Research: Solid Earth*, *121*(5), 3911–3938. https://doi.org/10.1002/2015jb012456

Martens, H. R., & Simons, M. (2020). A comparison of predicted and observed ocean tidal loading in Alaska. *Geophysical Journal International*, *223*(1), 454–470. https://doi.org/10.1093/gji/ggaa323

Martens, H. R., Simons, M., Owen, S., & Rivera, L. (2016). Observations of ocean tidal load response in South America from subdaily GPS positions. *Geophysical Journal International*, *205*(3), 1637–1664. https://doi.org/10.1093/gji/ggw087

Martinec, Z. (2000). Spectral–finite element approach to three-dimensional viscoelastic relaxation in a spherical Earth. *Geophysical Journal International*, *142*(1), 117–141. https://doi.org/10.1046/j.1365-246x.2000.00138.x

Matviichuk, B., King, M. A., Watson, C. S., & Bos, M. S. (2021). Limitations in one-dimensional (an) elastic Earth models for explaining GPS-observed M2 ocean tide loading displacements in New Zealand. *Journal of Geophysical Research: Solid Earth*, *126*(6), e2021JB021992. https://doi.org/10.1029/2021jb021992

Mooney, W. D., Laske, G., & Masters, T. G. (1998). CRUST 5.1: A global crustal model at 5×5. *Journal of Geophysical Research*, *103*(B1), 727–747. https://doi.org/10.1029/97jb02122

Müller, M. (2008). Synthesis of forced oscillations, Part I: Tidal dynamics and the influence of the loading and self-attraction effect. *Ocean Modelling*, *20*(3), 207–222. https://doi.org/10.1016/j.ocemod.2007.09.001

Pasyanos, M. E., Masters, T. G., Laske, G., & Ma, Z. (2014). LITHO1. 0: An updated crust and lithospheric model of the Earth. *Journal of Geophysical Research: Solid Earth*, *119*(3), 2153–2173. https://doi.org/10.1002/2013jb010626

Pekeris, C. L. (1975). A derivation of Laplace's tidal equation from the theory of inertial oscillations. *Proceedings of the Royal Society of London. A. Mathematical and Physical Sciences*, *344*(1636), 81–86.

Penna, N. T., Clarke, P. J., Bos, M. S., & Baker, T. F. (2015). Ocean tide loading displacements in Western Europe: 1. Validation of kinematic GPS estimates. *Journal of Geophysical Research: Solid Earth*, *120*(9), 6523–6539. https://doi.org/10.1002/2015jb011882

Platzman, G. W., Curtis, G. A., Hansen, K. S., & Slater, R. D. (1981). Normal modes of the world ocean. Part II: Description of modes in the period range 8 to 80 hours. *Journal of Physical Oceanography*, *11*(5), 579–603. https://doi.org/10.1175/1520-0485(1981)011<0579:nmotwo>2.0.co;2

Pugh, D., & Woodworth, P. (2014). *Sea-level science: Understanding tides, surges, tsunamis and mean sea-level changes*. Cambridge University Press.

Ray, R. D. (1998). Ocean self-attraction and loading in numerical tidal models. *Marine Geodesy*, *21*(3), 181–192. https://doi.org/10.1080/01490419809388134

Schaeffer, A. J., & Lebedev, S. (2013). Global shear speed structure of the upper mantle and transition zone. *Geophysical Journal International*, *194*(1), 417–449. https://doi.org/10.1093/gji/ggt095

Schindelegger, M., Green, J. A. M., Wilmes, S. B., & Haigh, I. D. (2018). Can we model the effect of observed sea level rise on tides. *Journal of Geophysical Research: Oceans*, *123*(7), 4593–4609. https://doi.org/10.1029/2018jc013959

Schwiderski, E. W. (1980). On charting global ocean tides. *Reviews of Geophysics*, *18*(1), 243–268. https://doi.org/10.1029/rg018i001p00243

Shihora, L., Sulzbach, R., Dobslaw, H., & Thomas, M. (2022). Self-attraction and loading feedback on ocean dynamics in both shallow water equations and primitive equations. *Ocean Modelling*, *169*, 101914. https://doi.org/10.1016/j.ocemod.2021.101914

Simms, A. R., Lambeck, K., Purcell, A., Anderson, J. B., & Rodriguez, A. B. (2007). Sea-level history of the Gulf of Mexico since the last Glacial maximum with implications for the melting history of the Laurentide Ice Sheet. *Quaternary Science Reviews*, *26*(7–8), 920–940. https://doi.org/10.1016/j.quascirev.2007.01.001

Stammer, D., Ray, R. D., Andersen, O. B., Arbic, B. K., Bosch, W., Carrère, L., et al. (2014). Accuracy assessment of global Barotropic ocean tide models. *Reviews of Geophysics*, *52*(3), 243–282. https://doi.org/10.1002/2014rg000450

Sulzbach, R., Dobslaw, H., & Thomas, M. (2021). High-resolution numerical modeling of Barotropic global ocean tides for satellite gravimetry. *Journal of Geophysical Research: Oceans*, *126*(5), e2020JC017097. https://doi.org/10.1029/2020jc017097

Takei, Y. (2017). Effects of partial melting on seismic velocity and attenuation: A new insight from experiments. *Annual Review of Earth and Planetary Sciences*, *45*(1), 447–470. https://doi.org/10.1146/annurev-earth-063016-015820

Takei, Y., Karasawa, F., & Yamauchi, H. (2014). Temperature, grain size, and chemical controls on polycrystal anelasticity over a broad frequency range extending into the seismic range. *Journal of Geophysical Research: Solid Earth*, *119*(7), 5414–5443. https://doi.org/10.1002/2014jb011146

Tanaka, Y., & Katori, H. (2021). Exploring potential applications of optical lattice clocks in a plate subduction zone. *Journal of Geodesy*, *95*(8), 1–14. https://doi.org/10.1007/s00190-021-01548-y

Tanaka, Y., Klemann, V., & Martinec, Z. (2019). Surface loading of a self-gravitating, laterally heterogeneous elastic sphere: Preliminary result for the 2D case. In *IX Hotine-Marussi symposium on mathematical geodesy* (pp. 157–163). Springer.

Tesauro, M., Kaban, M. K., & Aitken, A. R. (2020). Thermal and compositional anomalies of the Australian upper mantle from seismic and gravity data. *Geochemistry, Geophysics, Geosystems*, *21*(11), e2020GC009305. https://doi.org/10.1029/2020gc009305

Tesauro, M., Kaban, M. K., Mooney, W. D., & Cloetingh, S. (2014). NACr14: A 3D model for the crustal structure of the north American continent. *Tectonophysics*, *631*, 65–86. https://doi.org/10.1016/j.tecto.2014.04.016

Wang, H., Xiang, L., Jia, L., Jiang, L., Wang, Z., Hu, B., & Gao, P. (2012). Load love numbers and Green's functions for elastic Earth models PREM, iasp91, ak135, and modified models with refined crustal structure from Crust 2.0. *Computers & Geosciences*, *49*, 190–199. https://doi.org/10.1016/j.cageo.2012.06.022

Wang, J., Nigel, T. P., Clarke, P. J. C., & Bos, M. S. (2020). Asthenospheric anelasticity effects on ocean tide loading around the East China Sea observed with GPS. *Solid Earth*, *11*(1), 185–197. https://doi.org/10.5194/se-11-185-2020

Weis, P., Thomas, M., & Sündermann, J. (2008). Broad frequency tidal dynamics simulated by a high-resolution global ocean tide model forced by ephemerides. *Journal of Geophysical Research*, *113*(C10), C10029. https://doi.org/10.1029/2007jc004556

Wessel, P., & Smith, W. H. F. (1998). New, improved version of generic mapping tools released. *Eos, Transactions, American Geophysical Union*, *79*(47), 579. https://doi.org/10.1029/98eo00426

Whittaker, J. M., Goncharov, A., Williams, S. E., Müller, R. D., & Leitchenkov, G. (2013). Global sediment thickness data set updated for the Australian-Antarctic Southern Ocean. *Geochemistry, Geophysics, Geosystems*, *14*(8), 3297–3305. https://doi.org/10.1002/ggge.20181

Yamauchi, H., & Takei, Y. (2016). Polycrystal anelasticity at near-solidus temperatures. *Journal of Geophysical Research: Solid Earth*, *121*(11), 7790–7820. https://doi.org/10.1002/2016jb013316